

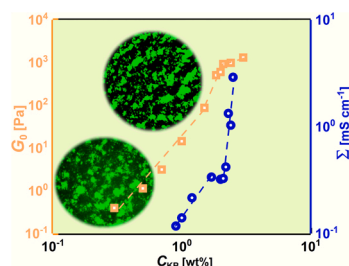
# Promising aqueous dispersions of carbon black for semisolid flow battery application

Mentallah Meslam<sup>a</sup>, Ahmed A. Elzatahry<sup>a</sup>, Mohamed Youssry<sup>b,\*</sup>

<sup>a</sup> Materials Science and Technology Program, College of Arts and Sciences, Qatar University, Doha 2713, Qatar

<sup>b</sup> Chemistry Program, Department of Chemistry and Earth Sciences, College of Arts and Sciences, Qatar University, Doha 2713, Qatar

## GRAPHICAL ABSTRACT



## ARTICLE INFO

### Keywords:

Carbon black  
Aqueous dispersions  
Suspension electrode  
Rheo-electrical properties  
Semisolid flow battery

## ABSTRACT

In this systematic study, we attempt to thoroughly understand the aggregation mechanism of conductive carbon black in aqueous dispersing medium and optimize the formulation of suspension electrodes for aqueous sodium-ion semisolid flow battery applications. For the first time, we present branched micelle solution as an electrolyte that introduces the widest electrochemical stability window of 3.5 V, from -3 to + 0.5 V vs. Ag/AgCl, with relatively low viscosity, rendering it as promising aqueous dispersing medium for suspension electrodes (anolytes). The simultaneous rheo-electrical measurements revealed that the aggregation of conductive ketjen-black (KB) particles was controlled by the electrostatic repulsion forces that doubly originate from the inter-aggregate soft interaction and bulk micelle interactions. This remarkable interaction rendered the dispersions electrically percolated at low carbon content (0.9 wt%) and importantly able to conserve the electrical conductivity under extremely high shear rates. Under the quiescent conditions, the percolated KB dispersion could sustain higher load of active material (up to 30 wt%  $\text{Na}_2\text{Ti}_3\text{O}_7$  as an active material) without severe influence on the rigidity (rheological plateau modulus  $G_0$ ) and electrical conductivity ( $\Sigma$ ) of the suspensions. These promising findings propound further investigation for the electrochemical performance of these aqueous sodium-ion suspension electrodes under flow conditions.

## 1. Introduction

After its advent in 1970s, redox flow batteries (RFBs) withdrew

significant interest as an alternative energy storage system due to design flexibility in separating energy and power in comparison to the conventional solid ion-batteries such as lithium-ion batteries [1]. The RFBs

\* Corresponding author.

E-mail address: [myoussry@qu.edu.qa](mailto:myoussry@qu.edu.qa) (M. Youssry).

<https://doi.org/10.1016/j.colsurfa.2022.129376>

Received 3 May 2022; Received in revised form 25 May 2022; Accepted 31 May 2022

Available online 3 June 2022

0927-7757/© 2022 The Author(s). Published by Elsevier B.V. This is an open access article under the CC BY license (<http://creativecommons.org/licenses/by/4.0/>).

encountered obstacles towards laying them efficient grid energy storage system due to their low energy density and low working potential [1,2]. Due to the relatively high cost-to-storage efficiency, the current RFBs account only for about 1% of the grid-scale energy storage merchandise. The need for large mass energy storage back-up systems for solar-farms or wind turbines plants, for instance grid storage applications, has renewed interest in another promising type of RFBs that can overcome the limitations encountered by conventional RFBs. Chiang et al. recently proposed a new concept; namely semi-solid flow battery (SSFB), which relies on replacing the dissolved electroactive ionic species used in conventional RFBs by electroactive solid particles suspended in a lithium-containing organic electrolyte and mixed up with conductive percolated carbon blacks [3]. Such semi-solid flow cell systems using flowing lithium-ion cathode and anode suspensions (catholytes and anolytes, respectively) allow: (i) increasing the energy density by a factor 10 compared to classical RFBs [3–7], (ii) increasing cell working voltage [8,9], (iii) improved stability [3,4], (iv) reducing gas formation [3,9], and (v) improving surface-electrolyte interface (SEI) formation [4, 9].

The aforementioned SSFBs and more utilized suspension electrodes composed of dispersed solid particles (lithium-based electroactive materials and conductive additives) in nonaqueous dispersing media (organic electrolytes of lithium salts). Because of economical, safety and environmental impacts, there is growing interest in replacing the nonaqueous media by alternative aqueous electrolytes. However, the water electrolysis at 1.23 V [10] and possible side reactions are unequivocally expected to limit the cell voltage and hence poor electrochemical performance. Few attempts have been reported to develop aqueous SSFB. Li and coauthors presented the first attempt of aqueous lithium-based SSFBs [11]. The battery displayed 202 Wh L<sup>-1</sup> at limited voltage of 0.9 V in 1 M LiNO<sub>3</sub> solution (at pH = 11–12). In recent study, Ventosa et al. introduced semi-solid hybrid flow battery which utilized aqueous solutions of ZnSO<sub>4</sub> and Li<sub>2</sub>SO<sub>4</sub> and showed a stability window of 1.65 V [12]. The aqueous electrolyte is still a serious constraint that suppresses the design of an efficient aqueous SSFB. Several approaches have emerged to extend the stability window of the aqueous electrolytes as reviewed recently [13]. Interestingly, Hou et al. endeavored to widen the working potential window of aqueous electrolytes through addition of surfactant molecules [14]. The authors successfully extended the stability window of an aqueous electrolyte to ca. 2.5 V and ascribed this behavior to the preferential adsorption of amphiphilic molecules created large energy barrier that impeded the mobility of water molecules toward the electrode surface. In the current study, we introduce a novel aqueous electrolyte relies on the so-called branched micelle solution. This structured fluid is characterized by its low viscoisty and higher diffusivity of ions and expectedly impart a colloid stability to the suspension electrodes.

Lithium-based SSFBs withdrew significant attention due to the well-established knowledge of chemistries and electrochemical performance of lithium-based electrode materials in stationary lithium-ion batteries. As a consequence of limited supply of lithium [15], and the smaller interaction potential of sodium (in comparison to that of Li) [16], there is a growing interest in exploration alternative material chemistries based on low cost and abundant ions such as sodium, which are highly desired for large-scale energy storage systems. Recently, Ventosa et al. presented a prototype of Na-ion SSFB containing anolyte and catholyte of Na-based active materials which displayed an energy density of ca. 9 Wh L<sup>-1</sup> [12]. Such limited density was attributed to the large overpotential of suspension electrodes which can be enhanced by proper selection and optimizing of the electrolyte, active materials (especially the catholyte) and cycling conditions.

Among significant amount of anode materials, titanium-based nanomaterials have attracted immense interest in the last decade due to their faster Na ion diffusion, efficient storage activity, high cycle stability, low operation voltage, low cost, facile synthesis, and environmental issue [17,18]. Specifically, sodium titanates (Na<sub>2</sub>Ti<sub>n</sub>O<sub>2n+1</sub>)

have been regarded as potential anode materials after the pioneer work of Tarascon in 2011 [19]. Particularly, sodium trititanate (Na<sub>2</sub>Ti<sub>3</sub>O<sub>7</sub>) and hexatitanate (Na<sub>2</sub>Ti<sub>6</sub>O<sub>13</sub>) gained considerable interest as anode materials with theoretical capacities of 178 mAh g<sup>-1</sup> and 99 mAh g<sup>-1</sup>, respectively [20]. These materials have a common high-aspect ratio morphology diverse from cuboids [21], nanotubes to nanofibers [22] structure. In the current study, the polymorph Na<sub>2</sub>Ti<sub>3</sub>O<sub>7</sub> has been selected as a model anode material to examine our approach when mixed with conductive additives; namely carbon black.

Conductive additives (e.g. carbon blacks (CBs)) are the second dispersing solid particles that affix the electrical conductivity of suspension electrodes when a three-dimensional “percolated” conductive network is formed above the percolation threshold (which depends on the particle size, surface area and chemistry of CB and its compatibility with solvent and active materials). Such network breaks up and the suspension loses its conductivity at critical: i) active material concentration in the stationary conditions, and ii) shear rate (flow rate) in the flow conditions [6,7]. To bypass these limitations, Youssry et al. proposed using hybrid carbon materials composed of carbon black and trace amount of filamentous carbon nanofibers (CNFs) in order to guarantee wiring the CB network so that it can sustain higher loading of active materials and recover the loss in electric conductivity under flow conditions [7].

In this study, we propose the utilization of aqueous electrolyte as a dispersing medium to understand the aggregation mechanism of conductive additive (ketjenblack; KB) and its percolating threshold in order to formulate aqueous suspension electrode (anolyte) for sodium-based semisolid flow battery. This aqueous electrolyte (branched micelle solution) has high degree of structuring facilitating the Na<sup>+</sup> diffusion [23] and is expected to colloidal stabilize the dispersions/suspensions and sustain higher load of active materials to eventually possess higher concentration of Na ions. Sodium-ion electrode active materials (Na<sub>2</sub>Ti<sub>3</sub>O<sub>7</sub>) with high theoretical capacity and highly conductive carbon blacks (KB) will be systematically dispersed in the branched micelle solution. This is to precisely determine the optimal composition (equilibrium) and operational conditions (under flow) for aqueous anolytes for aqueous sodium semi-solid flow batteries.

## 2. Experimental

### 2.1. Materials

Ketjen black EC600JD (KB; density = 1.90 g cm<sup>-3</sup>, BET surface area = 1270 m<sup>2</sup> g<sup>-1</sup>, primary particle size = 34 nm) was a gift from Lion Speciality Chemicals Ltd., Japan. Cetylpyridinium chloride monohydrate (CPyCl; purity 99.0 – 102%), titanium (IV) oxide anatase (TiO<sub>2</sub>, ≥ 99%), and anhydrous sodium carbonate (Na<sub>2</sub>CO<sub>3</sub>, ≥ 99%) were purchased from Sigma-Aldrich, USA. Sodium salicylate (NaSal, > 99.0%) was used as supplied from Surechem Products Ltd., UK. The sodium titanate (Na<sub>2</sub>Ti<sub>3</sub>O<sub>7</sub>; NTO) was synthesized and characterized as detailed in the [Supplementary materials](#) (Section S.1 and [Figs. S1](#)).

### 2.2. Preparation of dispersions

First, stock solution of branched micelles (aqueous electrolyte) was prepared by mixing aqueous solutions of CPyCl (0.1 M) and NaSal (0.1 M) in deionized water. The KB dispersions and suspension electrodes were prepared by ball-milling method. Weighted amounts of the solid materials (KB, NTO) and the branched micelle solution were transferred onto 15 mL–agate jar with 5–agate balls (∅ 6 mm) and mixed at 500 rpm for 3 h at room temperature.

### 2.3. Microscopy

The morphology of materials was investigated by transmission electron microscopy (TEM) from JEOL (100 CX), Japan. Scanning

electron microscope (SEM) from FEI Nova NanoSEM was used to study the morphology of the as-synthesized NTO and the suspension electrodes. Optical polarized microscope (Opto-Edu (Beijing) Co., Ltd, China) was used to inspect the dispersions homogeneity and structure.

#### 2.4. Rheology

The rheological properties of dispersions and solutions were carried out using a stress-controlled rheometer (Anton Paar MCR 102) equipped with plate–plate geometry (plate diameter 25 mm, gap 1 mm). All measurements were done at constant temperature 25 °C, controlled by Peltier system. To ensure the consistency, the rheological measurements followed a common protocol as follow: (i) the samples were pre-sheared at 100 s<sup>-1</sup> for 10 min, then left to relax for 5 min, (ii) the linear viscoelastic region was defined by strain sweep test, (iii) the frequency sweep test at an amplitude (from strain sweep) was recorded, and (iv) the flow curve (viscosity vs. shear rate) was acquired. A step rate test was conducted to simultaneously study the electrical behaviour of dispersions at particular shear rates (defined from the flow curve), with waiting time of 15 min at each shear rate.

#### 2.5. Electrochemical characterization

Electrochemical impedance spectroscopy (EIS) of dispersions and cyclic voltammetry (CV) of the aqueous electrolyte (branched micelle solution) were performed by a potentiostat/galvanostat (Squidstat Plus, Admiral Instruments, USA) at ambient temperature. A three–electrode cell configuration (glassy carbon as a working electrode, Pt/Ti wire as a counter electrode and Ag/AgCl as a reference electrode) was used to study the cyclic voltammetry at a scan rate of 10 mV s<sup>-1</sup>. Simultaneous EIS measurements (at rest and under flow) were conducted using the rheometer equipped with a customized copper plate–plate geometry (plate diameter 25 mm, gap 1 mm) connected with the potentiostat as shown in Fig. S2. The EIS spectra of KB dispersions and suspension electrodes were collected at 100 mV (the linear regime). The spectra, represented by Nyquist plots, were fitted to an equivalent circuit (depicted in Fig. S4) using EC-Lab® software (Biologic, France). The electrical resistivity of dispersions was used to calculate the electrical conductivity considering the geometrical parameters.

### 3. Results and discussion

#### 3.1. Branched micelle solution as an electrolyte

Branched (interconnected) micelle solution is a peculiar structured phase that is commonly formed in cationic surfactant systems [24]. Among various systems, the cationic surfactant; cetylpyridinium chloride (CPyCl) forms a branched micelle phase when mixed with a penetrating salt; sodium salicylate (NaSal) at high concentration [24,25]. The branched micelle solution is distinguished by its high fluidity, enhanced diffusivity of ions and thermodynamics stability. Such unique features render the CPyCl/NaSal solution as an excellent aqueous electrolyte (dispersing medium) for sodium semi-solid flow battery. Moreover, it has been reported that micelle-based electrolytes exhibited excellent electrochemical stability in comparison to common aqueous electrolytes [26,27].

In this study, various branched micelle solutions of CPyCl/NaSal system (varying CPyCl/NaSal molar ratio) have been examined electrochemically and rheologically. Among them, an optimal solution at 0.1 M CPyCl and 0.1 M NaSal is selected to be a dispersing medium for electrode formulation. This solution displays a Newtonian behavior with zero-shear viscosity ( $\eta_0$ ) of ca. 350 mPa s at 25 °C (data not shown). The electrochemical stability range of the micelle solution has been assessed by cyclic voltammetry at ambient temperature as depicted in Fig. 1a. The first cycle reveals electrochemical stability over a potential range from -3 V to +2 V before the onset of O<sub>2</sub> evolution above +2 V (inset of Fig. 1a). Though the voltammogram does not display any feature for anodic peak, weak cathodic peak appears at ca. -0.4 V. In the successive cycles, two anodic peaks continuously appear at +1.0 and +2.0 V whilst a cathodic peak is shifted to ca. -1.9 V in the reverse sweep (Fig. 1a). This electrochemical behavior is attributed to the redox reaction of salicylate ion designated by an anodic peak at +1.0 V in accordance with previous reports [28–31]. The second peak at +2.0 V is likely to ascribe to the adsorption of oxidation products on the glassy carbon electrode [30,32]. The dimeric oxidation products may form stable film on the electrode so that the cathodic peak is shifted to more negative potential at -1.9 V. In the first cycle, the oxidation of salicylate ion does not reach the steady-state [30] and hence unstable adsorbed film of oxidation products does not form. This may explain the lack of anodic peaks and reduction at lower potential (-0.4 V) in the first cycle.

As depicted in Fig. 1b, no obvious redox peaks were observed when the aqueous electrolyte was subjected to several cycles from -3.0–0.5 V;

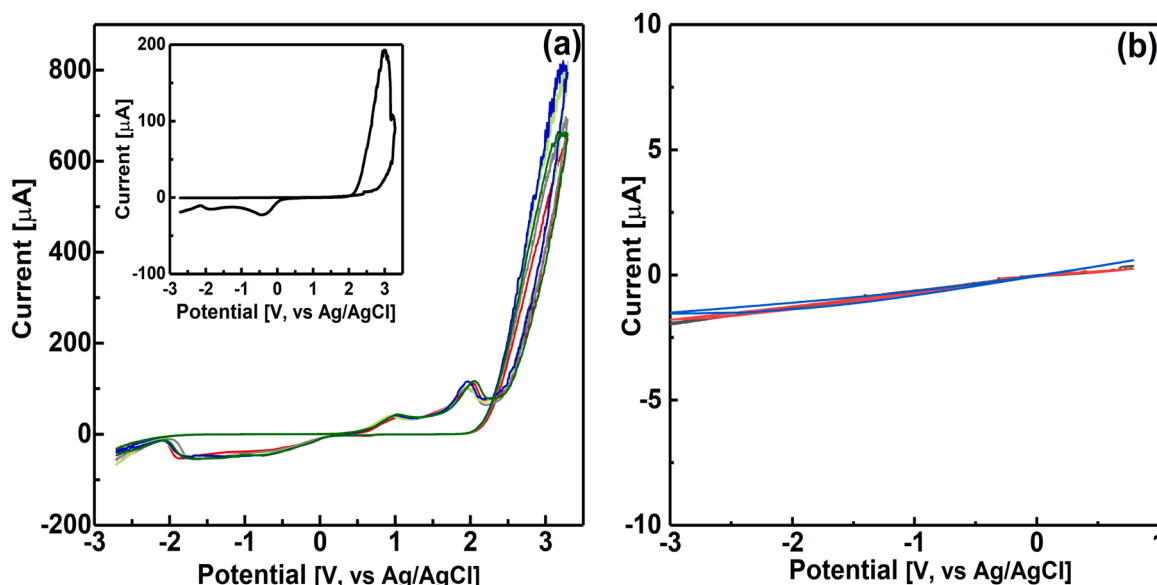


Fig. 1. Cyclic voltammograms of the branched micelle solution (0.1 M CPyCl + 0.1 M NaSal), at a scan rate of 10 mV s<sup>-1</sup> and ambient temperature.

before the anticipated oxidation at +1.0 V. The electrolyte exhibited striking electrochemical stability over this potential range, rationally without formation of dimeric film. Interestingly no indication for H<sub>2</sub> evolution up -3 V, whilst the O<sub>2</sub> evolution arises above +2 V, implying that no water hydrolysis over unusually extended potential window (5 V for the full scan or 3.5 V for the limited scan before the oxidation +1.0 V). Indeed, such potential window is extremely larger than the thermodynamic electrochemical stability window of water (1.23 V). It should be noted that the electrochemical decomposition is not only thermodynamically controlled but kinetic factors, such as scan rate, electrolyte concentration, and electrode type and surface, have significant impact on the stability window [33]. Previous studies reported strikingly wide electrochemical stability windows of 3.0 V [34] and 4.1 V [35] for aqueous concentrated electrolytes of ionic liquids, and 2.8 V for multi-component system [36].

The relatively low viscosity at moderate concentration of Na<sup>+</sup> and extended electrochemical stability window render this branched micelle solution (0.1 M CPyCl + 0.1 M NaSal) an excellent dispersing medium for the formulation of suspension electrodes for aqueous sodium-ion semisolid flow battery. The formation, adsorption nature and stability of dimeric film (oxidation products) might be pivotal factors that determine the electrochemical performance of electrode suspension. Accordingly, over which potential window (3.5 V vs 5 V) does the electrode efficiently operate? This is the objective of future study.

### 3.2. Aqueous dispersions of ketjen black

The electrical conductivity of suspension electrode arises from the three-dimensional network that is built up above a critical content of the conductive additive; namely the percolating threshold. The percolated conductive network is expected to sustain high load of electrically insulated active material and retain its conductivity under flow. Accordingly, it is worth to systematically determine the percolating threshold and investigate the rheological and electrical properties of the conductive additive (ketjen black; KB) in the branched micelle solution.

#### 3.2.1. Zeta potential of ketjen black in branched micelle solution

It is vital to explore the colloidal state of carbon black (KB) in the dispersing medium (branched micelle solution) in order to understand their aggregation mechanism and consequently the bulk mechanical and electrical properties. This can be accomplished by examining the zeta potential ( $\zeta$ ) values. Carbon black particles are known to carry negative a surface charge due to deprotonated oxygen-containing functional groups, so they form colloidal stable dispersions [37]. The dispersion of KB in deionized H<sub>2</sub>O shows  $\zeta = -35 \pm 2.56$  mV, implying that the surface of KB particles is negatively charged due to ionized surface oxygen functional groups in H<sub>2</sub>O. In NaSal aqueous solution, the KB particles still carry negative charge but the absolute value of zeta potential decreases ( $\zeta = -25 \pm 1.90$  mV) in comparison to pure H<sub>2</sub>O. This mild decrease may ascribe to charge neutralization due to the poor adsorption of Na<sup>+</sup> on the surface of carbon particles [37]. The KB dispersion in 0.1 M CPyCl significantly exhibits zeta potential  $\zeta = +50 \pm 1.25$  mV. The cationic surfactant tremendously changes the absolute value and charge of zeta potential. This charge inversion is likely to attribute to adsorption of the cationic surfactant on the carbon surface. Since the concentration of surfactant exceeds its critical micelle concentration (ca. 1.0 mM at 25 °C), it is rational to anticipate the formation of self-assembled layer or hemimicelles on the carbons surface [38,39]. The zeta potential of KB in the branched micelle solution (0.1 M NaSal + 0.1 M CPyCl) is unusually highly positive that may scarcely attribute to extremely high electrostatic repulsive potential energy induced by the bulk branched micelles. The effect of depletion interactions induced by micelles may contribute to the DLVO potential and results in uncommon extended double layer [40]. Moreover, the thickness of the adsorbed-surfactant layer and or the double layer around the KB particles cooperatively increase the effective volume fraction of particles [41,42].

Accordingly, long-range electrostatic repulsive forces dominate so that the particles rearrange in more compact aggregates [43]. It should be noted that the ionic conductivity of dispersions in both NaSal and branched micelle solutions is almost the same (ca. 7.0 mS cm<sup>-1</sup>), and higher than that in CPyCl solution (ca. 1.0 mS cm<sup>-1</sup>), which may be linked with high amount of Na<sup>+</sup> that are freely diffuse in the bulk medium.

#### 3.2.2. Dynamic rheology of aqueous KB dispersions

First, the dynamic strain sweep test was performed to determine the linear viscoelastic region (LVR) over which a minimal disturbance for the microstructure of dispersions is applied. The dilute dispersions (KB content;  $C_{KB} < 0.3$  wt%) generally pursue a typical viscous behavior, where the viscous modulus ( $G''$ ) is higher than the elastic modulus ( $G'$ ) over the entire shear strain ( $\gamma$ ) range (Fig. S3). Fig. 2a demonstrates strain sweep results for selected KB dispersions at higher content ( $C_{KB} \geq 0.5$  wt%). It is rational to recognize a continuous increase in the magnitudes of the dynamic moduli as  $C_{KB}$  increases. At  $C_{KB} \geq 0.3$  wt%, the dispersions generally show a gel-like response at low strain where  $G'$  is higher than  $G''$  and both viscoelastic moduli are nearly independent of  $\gamma$ , implying the formation of structured dispersions (data not shown for 0.3 wt% KB). Upon further deformation, the dispersions exhibit a deviation from LVR where  $G'$  starts to progressively diminish, whilst  $G''$  displays a maximum; the so-called strain-overshoot [44]. The strain-overshoot phenomenon has been observed in wide range of suspensions including carbon nanofibers [45,46], fumed silica [47], and soft glass [48]. It has been ascribed to the transition from viscoelastic dissipation (solid-like) to plastic flow (liquid-like) [49], associated with intrafloc deformation and interfloc dissipation [50], respectively. Beyond the LVR, the deformation initially disrupts the interaction between the carbon flocs (aggregates) resulting in discrete flocs that suffer viscoelastic dissipation. Further deformation is likely to gradually lessen the flocs size and smaller flowable particles are formed at very high strain. The extent of strain-overshoot is sensitive to the flocs size, extend and strength of interaction between flocs. Therefore, the phenomenon is more pronounced as the KB content increases (Fig. 2a), analogous to the behavior of CNFs dispersions [45].

At a critical strain ( $\gamma_c$ ), the KB dispersions exhibit  $G'-G''$  crossover beyond which the dispersions perform liquid-like behaviour where  $G''$  is higher than  $G'$  and both moduli diminish with the applied strain. Further reduction in the interaction between flocs and flocs size are likely to result in a liquid-like rheological behavior under higher deformation. Fig. 2b displays the dependency of  $\gamma_c$  on  $C_{KB}$ , described by the power law:  $\gamma_c \sim C_{KB}^\alpha$ , with two different exponents ( $\alpha$ ) revealing two distinct regimes. First,  $\gamma_c$  monotonically increases with KB content, showing positive exponent;  $\alpha = 2.5$ , in agreement with the scaling behavior for a network with weak interfloc links [51]. Similar exponent has been reported in previous study on analogous carbon black suspensions [52], contrary to the negative exponents reported for aqueous CBs [46] and nonaqueous CNFs [45] dispersions in ionic liquid. Interestingly, this unusual trend in the semidilute regime may ascribe to the progressive intensifying of the interaction between the flocs as a consequence of increased effective volume fraction of flocs as the KB content rises [41, 42]. The assumption of increased bond strength (rigidity) is excluded and the dispersions network is likely to reach the saturation state with strongly interacted (anisometric) aggregates at 1.5 wt% KB. Beyond this concentration, a second regime emerges where  $\gamma_c$  weakly decreases with KB content, displaying negative exponent;  $\alpha = -0.4$  (Fig. 2b). This trend in turn seems to be linked with a dense KB network formed from highly interacting flocs with presumably strong interfloc bonds [51] or different aggregation mechanism. Similar negative exponent has been reported for aqueous dispersions of CBs at low concentrations [46], and long carbon nanotubes [53] and in agreement with the theoretical exponent predicted for suspensions of interconnected network with bonds that freely rotate and resist stretching [54].

Profound understanding for the development of dispersions

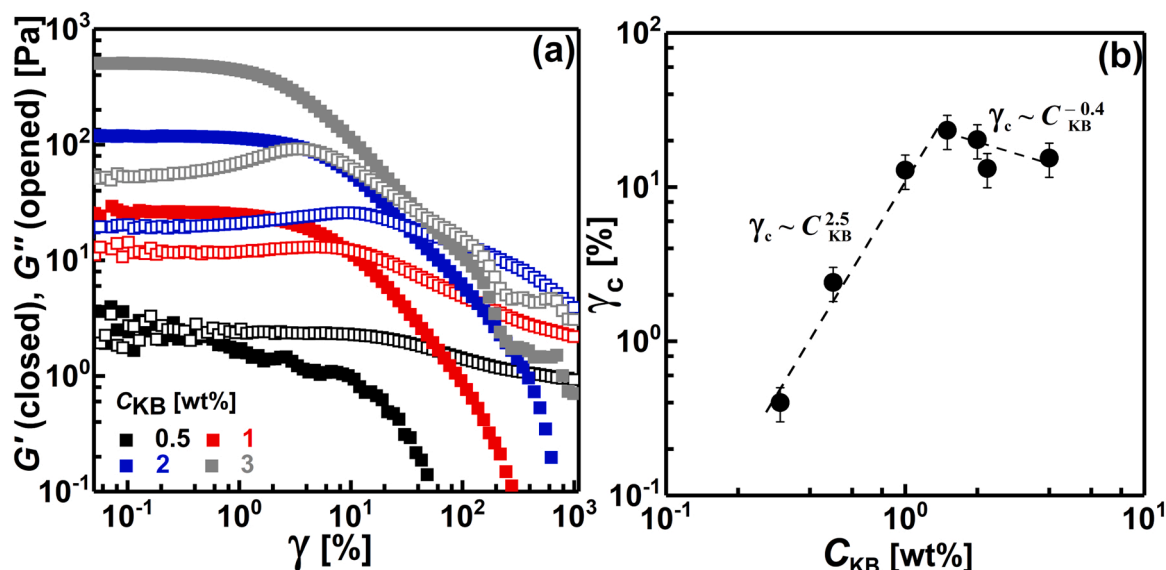


Fig. 2. (a) Strain sweep results for selected dispersions of carbon black (KB) in the aqueous electrolyte at 25 °C, 1 Hz, and (b) variation of the critical strain ( $\gamma_c$ ) with the concentration of carbon black ( $C_{KB}$ ).

microstructure is gained from the dynamic frequency sweep experiments at minimal perturbation (viz. in the LVER). Fig. 3 shows the frequency sweep results for selected dispersions over wide range of KB content. Initially, the dilute dispersions ( $C_{KB} < 0.3$  wt%) display a typical liquid-like response where  $G' > G''$  and both moduli are dependent of the angular frequency ( $\omega$ ), as shown in Fig. 3a. This implies that no structured dispersions have been yet formed and discrete KB flocs exist. The semidilute and concentrated KB dispersions otherwise start to exhibit gel-like viscoelastic response at  $C_{KB} \geq 0.3$  wt%, as can be seen from Fig. 3b. The semidilute dispersions (0.3–1 wt% KB) reveal unusual viscoelastic response that is scarce for analogous colloidal dispersions if they are physically structured. At low  $\omega$ ,  $G'$  is slightly higher than  $G''$  and nearly independent of the frequency until a critical frequency ( $\omega_c$ ) at which the dynamic moduli crossover, and then the dispersions behave a typical liquid-like response as revealed from the domination of  $G''$  over higher  $\omega$ . The frequency-dependency of  $G''$  is explicitly observed beyond  $\omega_c$ . Moreover,  $\omega_c$  is shifted to higher values as

$C_{KB}$  is increased from 0.3 to 1 wt%. Considering that the dispersions are viewed as weak network of flocs interspersed by the dispersing medium [55], the viscoelastic behavior of such semidilute KB dispersions may arise from two contributions. The elastic contribution at low  $\omega$  is mainly due to the long-range interaction forces between KB flocs in the network, whereas the Newtonian dispersing medium dominates the viscoelastic behavior at higher  $\omega$  ( $\omega > \omega_c$ ), regardless the KB content [55]. This picture is only adequate to describe the tenuous microstructure of dispersions at 0.3–0.5 wt% KB. At  $C_{KB} = 1$  wt%, the dynamic moduli, in comparison, increase by one decade with  $G' > G''$  and the relaxation frequency ( $\omega_c$ ) shifts to higher value (Fig. 3b). This behavior may attribute to the change in the size and morphology of flocs so that the floc-floc interaction strongly increases, rendering the dispersion network highly elastic. The nature of interaction is likely to be of either electrostatic interaction due to increased effective volume fraction [41, 42] or formation of physical interconnections (branches) between the flocs. Specifically, the dynamics (fluctuations) of KB branches turns

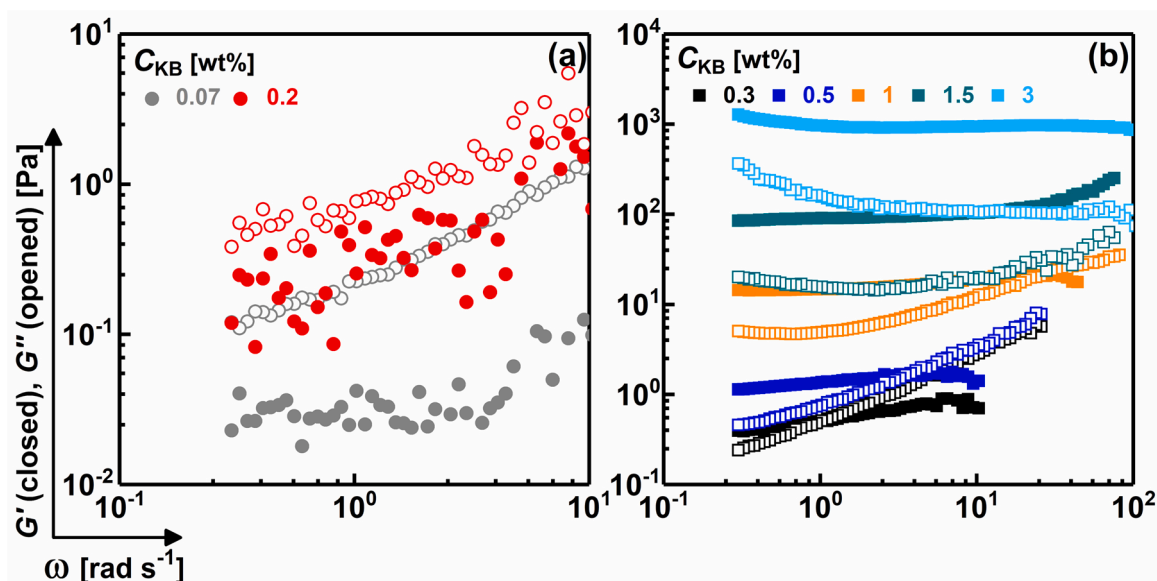


Fig. 3. Dynamic frequency sweep results (a) dilute dispersions (strain amplitude = 10%), and (b) concentrated dispersions (strain amplitude  $\leq 0.1\%$ ).

paramount at higher frequency, causing the moduli are dependent on the angular frequency [56]. Hence, the microstructure of semidilute dispersions (0.5–1 wt% KB) is likely to be weak gel with porous structure, analogous to dispersions of weakly attractive CB in mineral oil [52, 55] and aqueous microgel [57].

The 1.5 wt% KB seems to be a critical content where the dispersion differently exhibits a linear viscoelastic behavior typical for highly elastic network with strongly interacting flocs. It is signified by: higher magnitude of the moduli,  $G' > G''$  by one decade, frequency-independent  $G'$ , and disappearance of  $G' - G''$  crossover over the entire frequency range (Fig. 3b), implying that the structural relaxation time of this dispersion is larger than the duration of the experiment. This is likely to ascribe to intensively packed anisometric aggregates that reveal strong aggregate–aggregate interaction which results in poroelastic network rather than fluctuations of less flexible branches at high KB content [57]. In comparison to previous carbon black dispersions [6, 46, 58, 59], the KB in branched micelle solution reveals this peculiar viscoelastic behavior at lower carbon content which is considered advantageous for formulation of suspension electrodes. Above 1.5 wt% KB, the network grows into stiffer microstructure as revealed from the independency of both dynamic moduli on the frequency. For instance, the dispersion at 3 wt% KB displays linear viscoelastic response featured for highly elastic network (Fig. 3b). At low frequency, the gradual increase in  $G'$  and  $G''$  may delineates the reconstruction of gelation over the measuring time [60], since the measurement begins at high frequency (downscan) after full destructive strain sweep test.

To recap, the KB dispersions in branched micelle solution reveal unique microstructural development with KB content, where the dispersions: (i) are small discrete flocs below 0.3 wt%, (ii) begin to grow into larger flocs (agglomerates) showing a rheological weak gel at 0.3 wt % which span up to  $C_{KB} < 1.5$  wt%, and (iii) form saturated network at  $C_{KB} > 1.5$  wt%. Following this structural progression, the linear viscoelasticity is sensitive to the morphology and effective volume fraction of aggregates and hence the electrostatic interactions between aggregates that uniquely control the dynamic rheological behavior of KB dispersions. Further argument for the nature of microstructure of KB dispersions is additionally drawn from the electrical (impedance spectroscopy) behavior at equilibrium as discussed in Section 3.2.3.

Deeper discernment on the aggregation nature and mechanism in carbon dispersions is attained from the dependency of the rheological plateau modulus ( $G_0$ ) on the KB content, as depicted in Fig. 4a. At 0.3 wt % KB, the dispersions begin to exhibit a rheological elastic behavior with defined  $G_0$ . This critical concentration denotes the rheological

percolating threshold ( $C_r^*$ ) at which it is presumed that the flocs are interconnected (bonded) by carbon branches resulting in a percolated network spanning the dispersion [61, 62]. Nevertheless, the optical micrograph of the 0.3 wt% KB dispersion notably shows large incoherent aggregates without explicit sign of interconnections (Fig. 4b). As the KB content increased to 0.5 wt%, the agglomerates unambiguously transform from quasi-spherical to anisometric morphology (Fig. 4c). It should be stated that such lower percolating threshold (0.3 wt%) than that exhibited by carbon black dispersions in simple organic [6, 63] and aqueous [46] media is related to the formation of larger aggregates in micelle solution, in accordance with a recent simulation study [64]. As revealed from zeta potential measurements, the higher value and sign reversal (from negative to large positive) of zeta potential of KB dispersion in CPyCl/NaSal system is likely to attribute to formation of adsorbed surfactant layer or hemimicelles [38, 39, 65] on the carbon surface resulting in strong electrostatic repulsion forces. The strong interaction forces are likely to somewhat suppress the formation of carbon branches and discrete (quasi-spherical and anisometric) aggregates are alternatively formed rather than interconnected ones. Lu et al. reported a similar structural picture for sterically-stabilized colloidal dispersion with adsorbed short polymer [66].

Above  $C_r^*$ ,  $G_0$  monotonically increases with the KB content, exhibiting a power law relationship:  $G_0 \sim C_{KB}^\beta$  with two eminent exponents ( $\beta$ ) consistent with two regimes and varied microstructures. In the semidilute regime,  $G_0$  has a scaling exponent of  $\beta = 3.4$ , in accordance with the one reported for colloidal dispersions of carbon blacks [6, 52, 63], nanotubes [67] and silica nanoparticles [68, 69]. At  $C_{KB} > 1.5$  wt% (concentrated regime),  $G_0$  steeply increases with the KB content exhibiting higher scaling exponent;  $\beta = 6.9$  analogous to that reported for aqueous concentrated dispersions of carbon blacks [46], nanofibers [45], and nanotubes [53]. This trend is likely to ascribe to unusual aggregation mechanism consistent with distinct fractal dimensions around 1.5 wt% KB. In light of Shih model [51], the semidilute regime (0.3–1 wt % KB) is best described as a weak-link regime where the intrafloc links are stronger than the interfloc ones as revealed from the increase of both  $G_0$  and  $\gamma_c$  with KB content. In this regime, the fractal dimension ( $D$ ) of the flocs is related to the exponent  $\beta$  through Eq. (1) [51]:

$$D = 3 - \frac{1}{\beta} \quad (1)$$

The fractal dimension is found to be 2.7, much higher than the value predicted by Shih model ( $D \approx 2.1$ ) and reported for various dispersions in comparable concentration range [45, 55, 69]. This implies a different

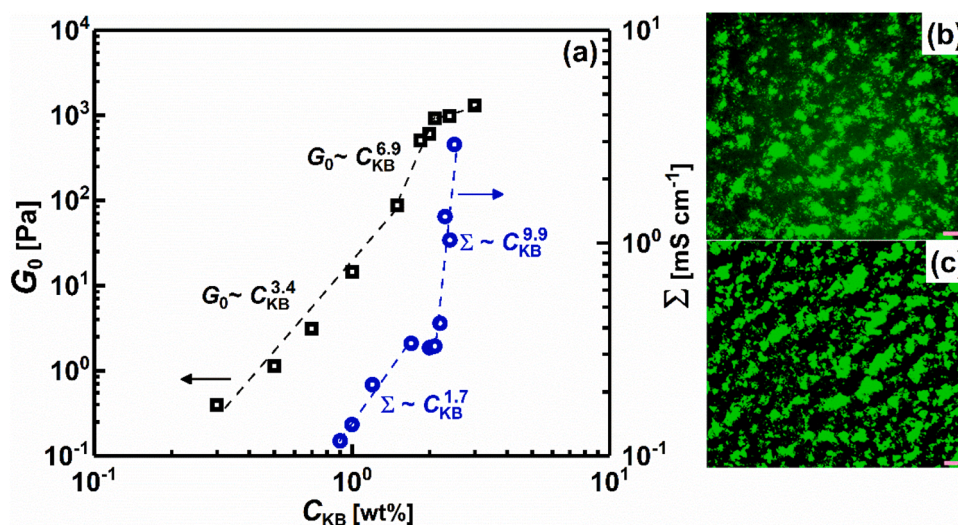


Fig. 4. (a) variation of plateau modulus ( $G_0$ ) and electrical conductivity ( $\Sigma$ ) with the concentration of KB ( $C_{KB}$ ) at 25 °C, and (b,c) optical micrographs of dispersions at 0.3 and 0.5 wt% KB, respectively. The dashed lines are the best linear fit, and the scale bars are 50  $\mu$ m.

aggregation mode, rather than the reaction limited cluster aggregation (RLCA) with  $D \approx 2.1$  [70,71]. In contrary, such fractal dimension is consistent with a ballistic particle cluster agglomeration (BPCA) mechanism where the hyperspherical flocs randomly combine to form larger aggregates exhibiting restructuring mechanism [72,73]. The strength of intrafloc links, number density of large anisometric aggregates (Fig. 4b, c) and restructuring-induced flexibility of aggregates [73] may delineate the elasticity of KB dispersions in micellar dispersing medium. The strong repulsion forces and the anisometry of aggregates are likely to be responsible for the compactification of aggregates and hence higher  $D$  value [66,74]. In comparison, similar  $D$  (2.6 – 2.7) values have been reported for highly concentrated dispersions of carbon blacks in aqueous [46] and organic [6,63] media, and polymeric mixture [66]. Richard et al. ascribed the elasticity of dispersions to the formation of dynamically arrested clusters induced by weak attractive or even repulsive forces that result in the domination of strong intrafloc links in comparison to small number and weak interfloc links [63]. Above 1.5 wt% KB, numerous flexible aggregates begin to rapidly coalesce [62] showing a sharp increase in the network elasticity as revealed from the large exponent of  $G_0$  ( $\beta = 6.9$ ). Using Eq. 1, the fractal dimension of the aggregates in the concentrated regime is found to be ca. 2.8, in agreement with the value reported for BPCA aggregation mechanism. Fully coalesced network with much higher compactifications is expected to display higher fractal dimension. However,  $D$  slightly increases from 2.7 (semidilute regime) to 2.8 (concentrated regime) approaching the maximum value of crystalline network ( $D=3$ ). This transition resembles a glass-like dynamical behaviour when the particle crowding effects are highly predominate [71] resulting in a fast gelation induced by coalescence [62]. This structural picture explains the decrease in the critical strain as the concentration increases beyond 1.5 wt% KB (Fig. 2b).

It is worth mentioning the sensitivity of the rheological properties of dispersions to the characteristics of carbon black (viz. surface area, particle size and surface chemistry) and the nature of the dispersing medium [75]. Particularly, the compatibility between KB and micellar solution plays a crucial role in controlling the aggregation threshold and mechanism and hence the microstructure of dispersion. Indeed, the KB is highly hydrophobic particles which are expected to rapidly flocculate in aqueous medium and shows a low rheological percolating threshold. Nevertheless, the branched micelle solution remarkably delineates the aggregation mechanism in a way that the microstructure is built by the unique ballistic-particle cluster agglomeration mechanism rather than

the other common mechanisms over limited concentration range. The strong electrostatic repulsive force induces the formation of (spherical and anisometric) aggregates with high effective volume fraction that strongly interact and densify to form percolated network at low carbon content. Coalescence and further densification of the network emerge at higher content of carbon black.

### 3.2.3. Electrical properties of aqueous KB dispersions

The evolution of equilibrium microstructure in dispersions can be plainly explored by the electrochemical impedance spectroscopy (EIS). The electrical resistivity due to the degree of structuring and networking of carbon dispersions is probed through this non-destructive test. Fig. 5 depicts the impedance spectra, represented by Nyquist plots, for selected KB dispersions. The dispersions at  $C_{KB} \leq 0.7$  wt% present nearly linear Nyquist plots analogous to that of the electrolyte (branched micelle solution), suggesting the predomination of the ionic conduction (Fig. 5a). Obviously, the rheologically percolated dispersions at 0.5 and 0.7 wt% KB do not show semicircles in their Nyquist plots, implying the lack of conduction pathways between the aggregates in agreement with the optical micrographs (Fig. 4b,c) and the structural conceive withdrawn from the rheological response.

At  $C_{KB} = 0.9$  wt%, the dispersion intriguingly begins to display a Nyquist plot with wide semicircle (in the high-frequency region) and linear tail (in the low-frequency region) as can be seen from Fig. 5b. The occurrence of semicircle indicates the building up of electrically conductive network in the dispersion at this critical content; namely the electrical percolating threshold ( $C_e^*$ ). As KB content increases, the semicircle gets narrower until nearly perfect semicircle appears at 1.5 wt% KB in tandem with the rheological viscoelastic behavior of dispersions. Nevertheless, it is noteworthy that the  $C_e^*$  is three-folded higher than  $C_r^*$ , that is certainly linked with the peculiar aggregation mechanism of KB in micelle solution. Below  $C_e^*$  (viz.,  $C_{KB} < 0.9$  wt%), the network is mechanically percolated due to progressively increased interaction between flowing units that confer the elasticity of the dispersions and render them to behave viscoelastic gel. The dispersions are electrically percolated at  $C_{KB} \approx 0.9$  wt% when the effective volume fraction and size of anisometric aggregates are large enough to form strongly interacted (connected) aggregates able to convey the electrical charges throughout the dispersion via hopping mechanism that does not requires physical interconnection [63,76]. This trend is consistent with the behavior of flocculated dispersions of carbon nanotubes [77–79]

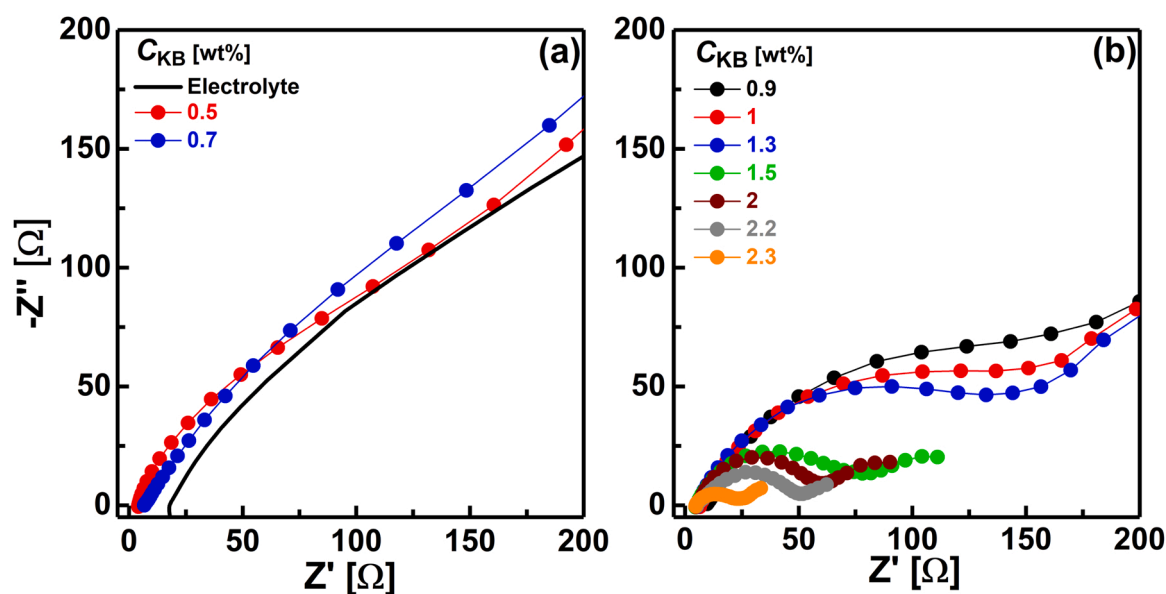


Fig. 5. Impedance spectra represented by Nyquist plots ( $Z''$ ; imaginary part of impedance versus the real part  $Z'$ ) for (a) diluted and (b) concentrated KB dispersions at ambient temperature.

which showed higher electrical percolating threshold than the rheological counterpart in contrast to the trend exhibited by analogous carbon blacks dispersions [46,63]. This discrepancy may ascribe to the varied aggregation mechanism in particular medium that is sensitive to the characteristics of dispersing particles and the nature of interaction in the dispersing medium.

A complementary quantitative evidence for the evolution of microstructure is acquired from the variation of electrical conductivity ( $\Sigma$ ) of dispersions with the carbon content as depicted in Fig. 4. The impedance spectra of dispersions are modelled by an equivalent circuit (Fig. S4) composed of ionic and electronic elements, as detailed in Section S.2. The dependency of  $\Sigma$  (calculated from Eq. S.1) on the KB content incontrovertibly confers further insight into the development of equilibrium microstructure of dispersions. Above the electrical percolating threshold ( $C_{KB} \geq 0.9$  wt%), the electrical conductivity monotonically increases with KB content (Fig. 4), showing a power-law relationship:  $\Sigma \sim C_{KB}^{1.7}$ , with an exponent comparable to the theoretical “universal” exponent (1.9) of percolated three-dimensional network [80] and the reported ones (1.7–1.8) for analogous conductive dispersion [6] and composites [81,82]. This exponent is assumed to be linked to the strength of transition and depends only on the dimensionality of the system [83]. Accordingly, such comparable exponent signifies the formation of peculiar network of interaction anisometric aggregates, rather than the conventional three-dimensional counterpart of physically interconnected aggregates. As the KB content increases, the network turns denser when the anisometric aggregates grow and strongly interact due to enhanced effective volume fraction. Above 1.5 wt% KB, the conductivity of the concentrated dispersions steeply rises with the KB content revealing unusual “nonuniversal” exponent of 9.9 (Fig. 4). Similar exponent has been shown by conductive composites of carbon blacks [84] and nanotubes [85], and is likely to indicate a structural transition above 1.5 wt% KB in accordance with the aforementioned behavior of the rheological plateau modulus. The nonuniversal conductivity exponent is related to a peculiar “tunnelling percolation mechanism” [86] when the system is composed of isolated aggregates (dispersed configurations rather than clustered ones [87]) with size larger than the tunnelling range [88]. This structural portrayal may similarly describe a coalescence network of large densified aggregates (as drawn from the rheological behavior) able to convey electrical charges through tunnelling mechanism. Such unusual structural development is likely to be linked with the structured dispersing medium that delineate the aggregation behavior. Brilloni et al. recently reported a model that describes the impact of electrolyte concentration on the aggregation/sedimentation behavior of carbon black dispersions [89]. The authors attributed the efficiency of electrical percolation to the shielding effect between carbon particles which is significant at high ionic strength.

In conclusion, the simultaneous rheological and impedance behaviors of KB dispersions in branched micelle solution revealed structural transition at a critical KB content. The semidilute percolated dispersions are composed of interacted aggregates which begin to electrically percolate at 0.9 wt% when the aggregates are enough highly anisometric and strongly interacting to convey the electrical current by hopping mechanism. The microstructure transforms into coalescence agglomerates above 1.5 wt% KB exhibiting tremendous rise in the electrical conduction induced by tunnelling mechanism. Further insight into the microstructural transformation under continuous shear flow is yet decisive to confirm such structural development.

### 3.2.4. Non-linear rheology of ketjen black dispersions

It is vital to investigate the effect of continuous shear flow on the KB dispersions and elucidate plausible shear-induced structural transitions and consequence change in the dispersions' conductivity. This can be achieved through examining the variation of steady shear viscosity ( $\eta$ ) and stress ( $\tau$ ) with the applied shear rate ( $\dot{\gamma}$ ) as depicted in Fig. 6. It is

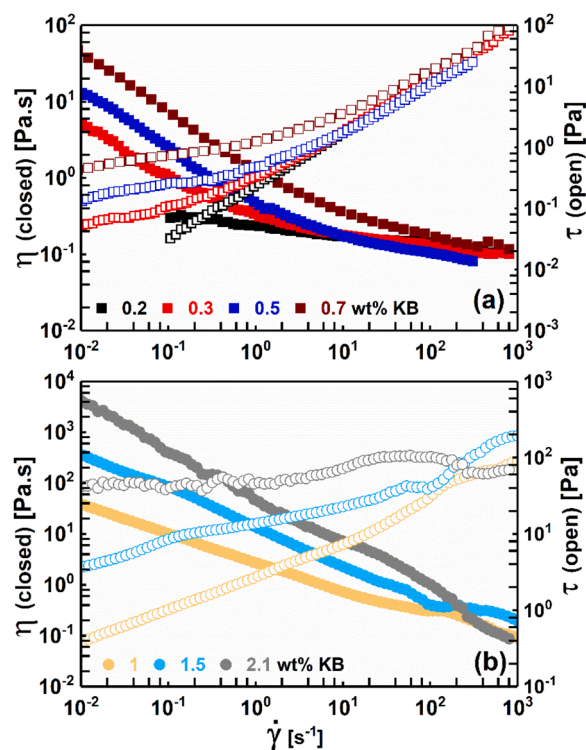


Fig. 6. Variation of shear viscosity ( $\eta$ ) and stress ( $\tau$ ) with shear rate ( $\dot{\gamma}$ ) for selected KB dispersions at 25 °C.

rational to conceive a continuous increase in  $\eta$  as the KB content rises. The dilute dispersions ( $C_{KB} \leq 0.2$  wt%) are typical Newtonian fluids since  $\eta$  is nearly independent of  $\dot{\gamma}$  over the entire range (Fig. 6a), implying that the dispersions are not yet structured in agreement with the dynamic rheology and impedance spectra at rest. The semidilute dispersions (0.3–0.7 wt% KB) initially exhibit a shear thinning behavior at low shear rates before they reveal an infinite shear viscosity (Newtonian) plateau over higher shear rates (Fig. 6a), analogous to the behavior of sterically stabilized dispersions [90,91]. Furthermore, no notable sign for shear thickening behavior is detected, in contrary to the behavior of similar structured dispersions [6,45,46,92,93] when a percolated network is formed. Accordingly, the structuring in the semidilute dispersions originates from randomly oriented large spherical (or anisometric) carbon aggregates [41,42] stabilized by strong repulsive forces due to the coated surfactant layers and the bulk branched micelles, rather than the formation of carbonaceous interconnections. Such complex (electrostatic and/or steric) interaction results in higher effective volume fraction than the core volume fraction of aggregates [42,43] so that the elasticity of dispersions are due to electrostatically and sterically interacted large aggregates. Beyond a critical stress (yield stress), the viscosity monotonically decreases when the stress is enough to overcome the interaction between aggregates and turns them disordered aggregates flowing with the plane of shear [43]. Above a critical shear rate, the viscosity is nearly independent of the shear rate in consistent with the linear rising of the shear stress, implying the Newtonian behavior of dispersions (Fig. 6a), which is consistent with the freely sliding of aggregates when the hydrodynamic interaction predominates [43]. As the KB content increases, the transition from thinning to Newtonian behavior is shifted to higher critical rates due to larger effective volume fraction and hence stronger interaction. The simultaneous impedance spectra under shear flow of semidilute dispersions (e.g. 0.5 wt% KB in Fig. 7a) do not show any traces of semi-circles over wide range of shear rate (in the thinning or the Newtonian regimes), implying the lack of physical carbonaceous interconnections (branches) to convey the electrical current either at rest ( $\dot{\gamma} = 0$  s $^{-1}$ ) or

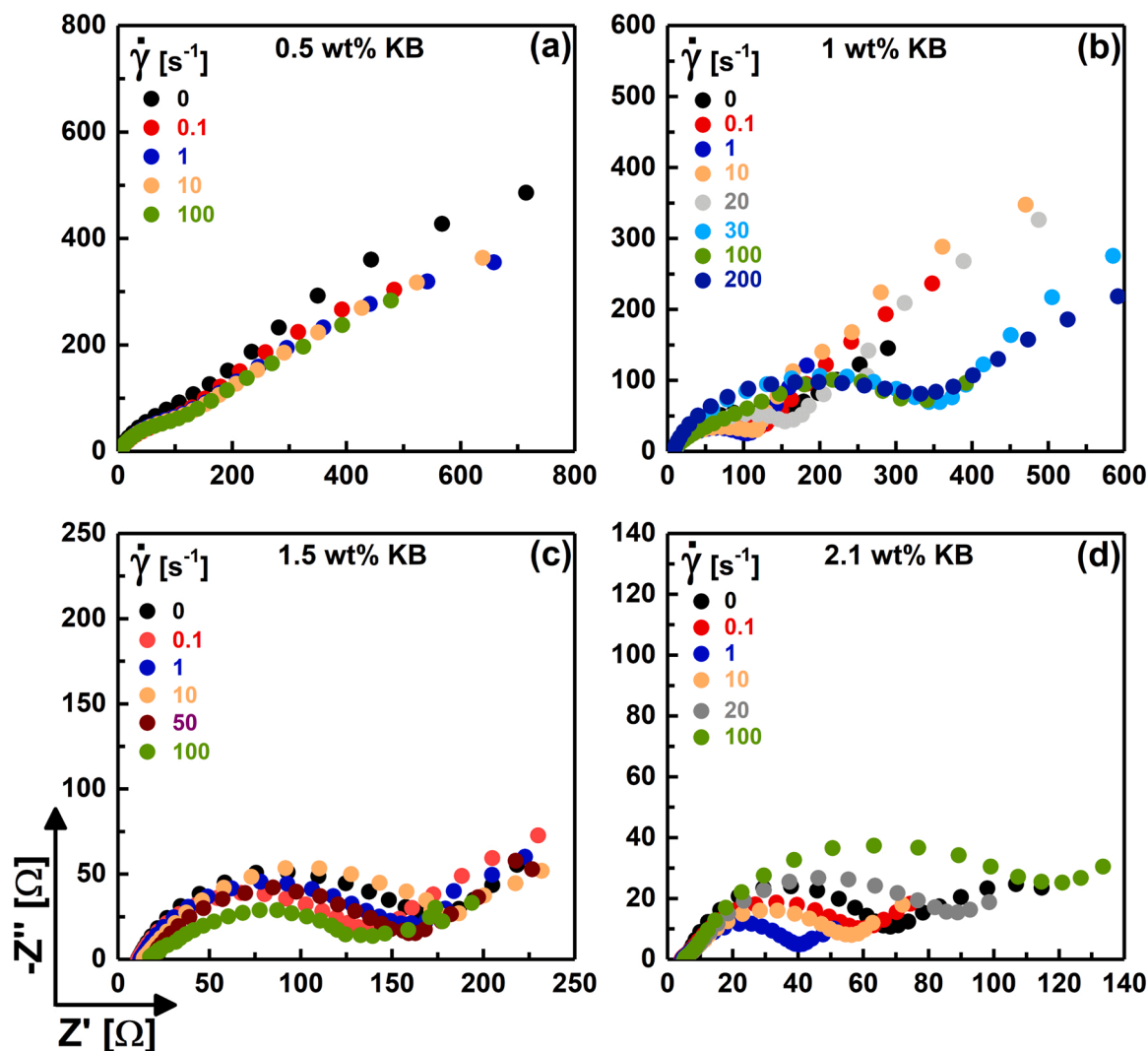


Fig. 7. Impedance spectra (Nyquist plots) of various KB dispersions under wide range of shear rates ( $\dot{\gamma}$ ), at 25 °C.

induced by shear flow ( $\dot{\gamma} > 0 \text{ s}^{-1}$ ); in other words, the dispersions are neither electrically percolated nor exhibit shear-induced percolation.

Intriguingly, at the end of semidilute regime (viz. 1 and 1.5 wt% KB), the dispersions commonly show three-regime flow curves characterized by two shear thinning regimes, separated by shear thickening regime (Fig. 6b), similar to the flow behavior that is previously reported for corresponding concentrated dispersions [6,45,46,58,94]. In comparison, we notice the domination of the first shear thinning over wider  $\dot{\gamma}$  range (up to ca. 20–50  $\text{s}^{-1}$ ) than that previously reported for similar carbon dispersions. Indeed, the shear thickening behavior is linked with the formation of physically interconnected aggregates [43,95,96]. Furthermore, the 1 and 1.5 wt% KB dispersions are electrically percolated due to the friction between anisometric aggregates with large effective volume fraction, as described aforementioned. Accordingly, the first shear thinning arises mainly from a decrease in the effective volume fraction so that the apparent size of aggregates may decrease with  $\dot{\gamma}$  [96]. This postulation is obviously evident from the continuous increase in the shear stress (Fig. 6b) which attempts to overcome the repulsive barrier due to long-range electrostatic repulsion forces. Above a critical  $\dot{\gamma}$ , the stress is high enough to presumably break up the aggregates and render them come into direct contact resulting in shear thickening regime at very high  $\dot{\gamma}$  ( $> 10^2 \text{ s}^{-1}$ ). The onset of shear thickening is shifted to relatively higher  $\dot{\gamma}$  as the KB content is increased from 1 to 1.5 wt%. This behavior is likely to be associated with the aggregate-crowding effect [71] when the dispersions approach the

glassy-like state. Furthermore, suppressing of shear thickening to higher  $\dot{\gamma}$  is mainly linked with the increased packing volume fraction of poly-disperse large aggregates [91,97] when the stress is enough to induce lubricated-frictional transition [98] causing an additional energy dissipation [42]. This prediction is qualitatively consistent with the simulation results of Melrose [99,100] who explored the influence of conservative repulsive forces on suppressing the onset of shear thickening to higher  $\dot{\gamma}$ . Further increase of  $\dot{\gamma}$  results in diminishing of the friction forces between the small aggregates, analogous to the relaxation of the constraint on the relative sliding motion between the aggregates, and eventually the second shear thinning transition emerges at higher  $\dot{\gamma}$  (Fig. 6b). This is consistent with the stress plateau when the density of aggregates remains constant at higher  $\dot{\gamma}$  [101].

As revealed from the dynamic rheology, the dispersions above 1.5 wt% KB have different structural state when the size and anisometry of aggregates change so that the neighbouring particles in the same aggregate fuse [62] in a similar pattern to the coalescence of emulsions [101]. The repulsive interactions between overlapping aggregates lead to an increase in the degree of compactness of large aggregates [70], resulting in higher elasticity. The coalesced dispersion at 2.1 wt% KB reveals three-regime flow curve as depicted in Fig. 6b. In comparison to the semidilute dispersions, the coalesced ones shear thickens over intermediate  $\dot{\gamma}$  range as revealed from the change in the slope of shear stress at ca. 10  $\text{s}^{-1}$ . This discontinuous shear thickening is typically exhibited by concentrated suspensions and is believed to arise from the

dilation and jamming of suspended particles when the frictional contacts between the aggregates dominate [102,103]. The thickening regime separates two shear thinning regimes. The low-shear rate thinning is likely to be associated with the shear-induced alignment of coalesced aggregates, analogous to highly concentrated dispersions [45]. This is consistent with the stress plateau at low shear rate range (Fig. 6b), which is dominated by entropic contribution comes from the distortions in the equilibrium structure [104]. Beyond the critical  $\dot{\gamma}$  of thickening, the shear stress increases as a result of strong frictional contacts between closely approaching aggregates [98]. Further increase of  $\dot{\gamma}$  results in second shear thinning regime, associated with unusual dropping of shear stress. This behavior is likely to arise from the cracking of jammed aggregates at very high shear rates, similar to the behavior of polymeric dispersions [105].

It is worth noting that the shear thickening is reversible process with negligible hysteresis in the upscan and downscan modes as depicted in Fig. S5 for selected dispersions in the semidilute regime (viz. 1 and 1.5 wt% KB). The reversibility of thickening has been investigated by simulation [106] and experiments [107–109] and ascribed to the formation of transient stress-bearing aggregates as a result of short-range hydrodynamic lubrication forces restraining the repulsive forces between aggregates during flow. The stress dependence of the aggregates interaction renders shear thickening reversible [110] and when the applied stress is removed, the dispersions relax back to the viscous state with negligible hysteresis. It can be advantageous to obtain conductive dispersion with reversible shear thickening behavior at high shear rate. This reversibility secures the stability of microstructure and hence any innocent variation of electrical conductivity of dispersions when operate in the flow cells.

### 3.2.5. Rheo-impedance of ketjen black dispersions

Further insight on the shear-induced structural transitions in KB dispersions can be precisely gained from the simultaneous measurements of the impedance spectra under constant shear rate. Fig. 7 demonstrates the variation of impedance spectra under step rates for selected semidilute (electrically unpercolated and percolated) and coalesced dispersions. As aforementioned, the 0.5 wt% KB dispersion revealed a viscoelastic gel-like response and non-Newtonian flow behavior under shear flow, indicating that the dispersion is rheologically structured. Nevertheless, its impedance spectra lack semicircles neither at rest nor under shear flow (Fig. 7a). Instead, the spectra are dominated by linear Nyquist plots, implying that the dispersion is electrically unpercolated. Obviously, the high effective volume fraction and hence electrostatically interacting aggregates results in rheologically percolated network that lacks any physical interconnections (branches) to convey electrical current. As a result, the dispersion is indeed viscoelastic weak gel with disordered flowing aggregates under continuous shear flow, however, it is purely ionic conductor. Well above the percolating threshold, the semidilute (1 and 1.5 wt% KB) and coalesced (2.1 wt% KB) dispersions are electrically percolated as delineated by their semicircle Nyquist plots at rest and under shear flow (Fig. 7b-d). The percolated dispersions commonly reveal variation of the diameter of semicircles with the shear rates. Qualitatively, they sustain the shear flow as revealed from the existence of nearly identical semicircles over wide range of shear rates ( $\dot{\gamma} \leq 20\text{--}50\text{ s}^{-1}$ ), before they relatively widen above critical shear rates ( $\dot{\gamma} \geq 20\text{--}50\text{ s}^{-1}$ ) that depend on the KB content. Further increase in the shear rate results in narrowing the semicircles again particularly for the semidilute dispersions rather than coalesced one. Analogous conductive dispersions showed nearly similar variation of impedance spectra under shear flow, consistent with shear-induced insulator-conductor transitions arose from structural transformations under flow [6,7,46]. In comparison, the striking feature of the impedance spectra of our percolated KB dispersions is the existence of semicircles over wider  $\dot{\gamma}$  range than those revealed by analogous dispersions in nonaqueous [6,7,45] or aqueous [46] media of ionic liquid. This implies the significant resistivity of percolated KB dispersions in branched micelle

solution to any undesirable structural transitions and hence loss of electrical conductivity under flow conditions.

Deeper insight on the plausible shear-induced structural transitions in KB dispersions can be quantitatively explored from the variation of the electrical conductivity with the shear rate, as depicted in Fig. 8. Surprisingly, the electrical conductivity of the percolated and coalesced dispersions are nearly independent of the shear rate, in consistent with the first shear thinning. This implies that the shear flow does not significantly alter the microstructure and the dispersions remain electrically conductive over wide  $\dot{\gamma}$  range. Such behavior is likely to be linked with rearrangement of aggregates under shear flow that causes change in the distribution of neighboring aggregate distances and orientations [103], rather than breaking up of microstructure. This is because the fundamental interactions between the aggregates that are responsible for the measured forces do not alter under shearing. It has been reported that different stress responses can be found for consistent microstructures, and large change in viscosity is not necessarily due to shear-induced structural transitions. For instance, colloidal dispersions exhibited strong (due to change in entropic forces) [104,111] and weak (due to change in viscous forces) [90] shear thinning behaviors as consequence of random particle arrangements. In general, the independency of electrical conductivity on the applied  $\dot{\gamma}$  is extended to slightly higher  $\dot{\gamma}$  as the KB content increases. Beyond a critical  $\dot{\gamma}$ , the electrical conductivity of the percolated dispersions (1 and 1.5 wt% KB) suddenly decreases with the shear rate and shows a slight minimum over relatively high  $\dot{\gamma}$  (Fig. 8a,b). Such drop in conductivity aligns with the shear thickening regime that can be described by the dilatancy mechanism [112] that features the thickening of densely packed particles. Upon shearing, the aggregates stretch (dilate) around each other

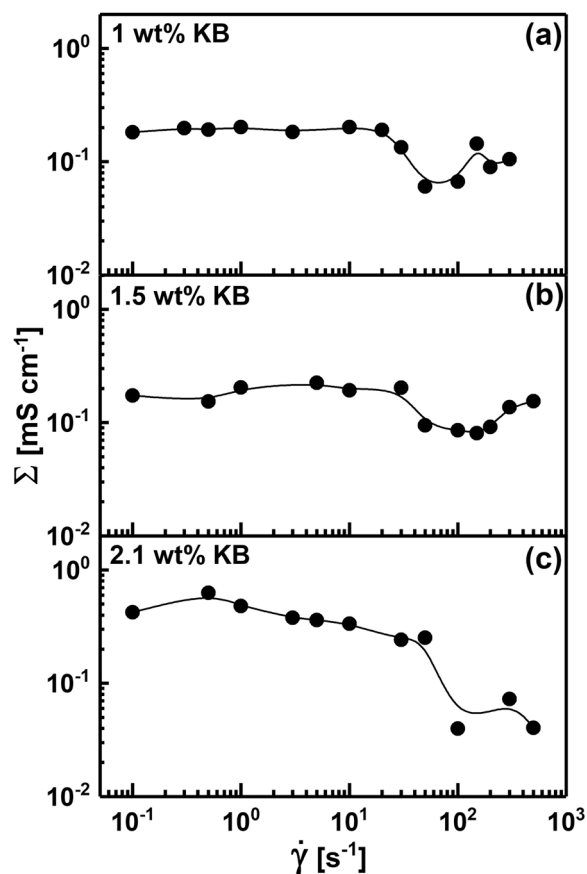


Fig. 8. Variation of the electrical conductivity ( $\Sigma$ ) with shear rate ( $\dot{\gamma}$ ) for (a,b) semidilute and (c) coalesced KB dispersions at 25 °C. The  $\Sigma$  values were calculated using the proposed equivalent circuit (Fig. S4) as described in Section S.2 in the Supplementary materials.

without taking direct paths, so their packing volume expands resulting in the increase of the dispersion viscosity (thickening) [103] and loss of conduction pathways for hopping. Further increase of  $\dot{\gamma}$  results in raising the electrical conductivity in tandem with the second shear thinning (Fig. 8a,b). This behavior is likely to arise from enough stress able to dynamically reconfigure the dilatant aggregates into aligned flowing units with sufficient frictional contacts to recover the electrical conductivity at very high shear rates. On the other hand, the coalesced dispersion (2.1 wt% KB) suffers strong loss of electrical conductivity beyond its critical  $\dot{\gamma}$  (Fig. 8c) in consistent with the thickening regime. This may results from the cracking of jammed aggregates that cannot rescue their connectivity even at higher shear rates and hence the conductivity irreversibly drops.

The rheo-electrical properties of KB dispersions evidently elucidated their rheological behavior under shear flow. Based on the fact that the dispersions are percolated due to electrostatically interacted aggregates, rather than physically interconnected ones, the low-rate thinning regime is mainly consistent with shear-induced orientation or alignments of aggregates. Such rearrangements do not seriously influence the electrical conductivity where the current conveys through hopping mechanism. Beyond the critical shear rate, the aggregates dilates exhibiting shear thickening behavior in tandem with loss of conductivity where the distance between flowing units are high enough to restrain the hopping mechanism, and the dispersions slightly lose their electrical conductivities. Additional stresses induce the alignment of dilatant aggregates, and getting them to closely approach in order to retain their conductivity. The coalesced dispersion nearly exhibits the same trend with serious cracking beyond the critical shear rate where the conductivity is not retained; at least over the examined shear rate range.

In general, the conductivity minimum of the semidilute dispersions is less pronounced than that exhibited by analogous carbon dispersions [6, 45] and nearly resembles that of hybrid carbons [7,45]. This implies that the KB dispersions in micelle solution strongly resist the deformation of microstructure under continuous flow conditions so that they remain electrically conductive even under very destructive flow conditions. This is an advantageous property for the conductive dispersion to safely operate under continuous flow conditions when mixed with the electrochemical active material to formulate the suspension electrode for semisolid flow battery.

### 3.3. Aqueous sodium – based suspension electrode

It is worth to examine the capacity of conductive dispersions to uptake electrically insulated active materials without severe impact on the flowability and electrical conductivity of formulated electrode suspensions. Initially, this aim is achieved via exploring the rheo-electrical properties of suspension electrode under static conditions. Sodium titanate ( $\text{Na}_2\text{Ti}_3\text{O}_7$ ; NTO) has been selected as a model anode material for anolyte formulation due to its relatively high theoretical capacity (ca.  $178 \text{ mAh g}^{-1}$ ) and low working potential [113]. The anolytes are formulated through a systematic addition of NTO to the percolated KB dispersion in order to assess the rheological and electrical properties under static conditions. The optimal anolytes are those with optimal rheological (flowable) and electrical (yet conductive) at highest NTO content.

Upon adding the electrically insulated active material to the percolated conductive dispersions, breaking up (or deteriorating) of the conductive pathways may takes place, resulting in serious loss of the electrical conductivity of anolyte. Moreover, undesired increase in the rigidity of the anolyte is likely to occur. Accordingly, it is rational to assess the influence of NTO content on the microstructure of anolytes made up of KB and NTO dispersed in branched micelle solution to precisely find out the optimal composition of NTO at which the suspension electrode is somewhat flowable and yet electrically conductive. In other words, to what extend (content of NTO) the percolated KB dispersion can sustain highest amount of NTO without serious loss of electrical

conductivity and increased elasticity under equilibrium conditions?

In comparison, semidilute (1.5 wt% KB) and coalesced (2.1 wt% KB) KB dispersions have been selected to examine the effect of added NTO on the microstructure (rheologically and electrically) of the resultant anolytes at rest. In general, the dynamic viscoelastic behavior of suspensions reveal gel-like response where  $G'$  is one-decade higher than  $G''$  over the entire frequency range (Fig. S6). While  $G'$  is thoroughly independent of the frequency,  $G''$  suffers slight dependency on the frequency for the NTO-1.5KB suspensions in comparison to NTO-2.1KB counterparts. This implies the increased strength of the suspension's network as a result of cooperative interaction due to strong packing of NTO particles in the KB aggregates. Similar dependency of the loss modulus has been exhibited by analogous suspensions [7], and may ascribe to the reorganization followed by weakening of the interaction (frictional contacts) between the carbon aggregates without significant influence on the rigidity of the suspensions [114]. At  $\text{NTO} \geq 25 \text{ wt\%}$ , the NTO-1.5KB suspensions turn stronger gel as revealed from the smaller difference (less than one decade) and weaker dependency of the dynamic moduli on the frequency (e.g. 25NTO-1.5KB suspension in Fig. S6-a).

The electrical behaviour of NTO-1.5 KB suspensions are in excellent agreement with their dynamic properties as revealed from the impedance spectra as depicted in Fig. S7. Upon addition of 5 wt% NTO to the 1.5 wt% KB, the characteristic semicircle of the conductive network becomes wider indicating the deterioration of the conductive pathways due to the added NTO particles that are embedded in the KB network. Further addition of NTO does not result in significant variation in the impedance spectra of suspensions over the entire NTO content (Fig. S7-a). On the other hand, the electrical behavior of NTO-2.1 KB suspensions supports this assumption where the semicircles of Nyquist plots strongly resemble that of the NTO-free KB dispersion with non-monotonic widening of the semicircles as the NTO content rises (Fig. S7-b).

Fig. 9 depicts a quantitative comparison for the effect of NTO content on the rheological  $G_0$  and electrical  $\Sigma$  parameters on the semidilute and coalesced networks at 1.5 and 2.1 wt% KB, respectively. On addition of small amount of NTO (3 wt%) to the 1.5 wt% KB,  $G_0$  strongly increases (one decade) in tandem with a small decrease in  $\Sigma$  (Fig. 9a). Further increase of NTO content does not significantly alter the network rigidity and electrical conductivity where  $G_0$  and  $\Sigma$  remain nearly constant up to

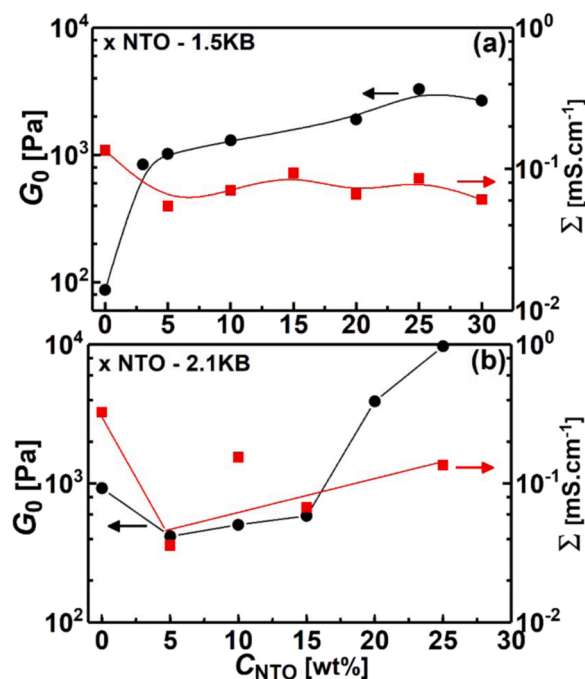


Fig. 9. Effect of NTO content ( $C_{\text{NTO}}$ ) on the plateau modulus ( $G_0$ ) and electrical conductivity ( $\Sigma$ ) of NTO-KB anolytes at (a) 1.5 and (b) 2.1 wt% KB.

higher NTO content. This behavior may arise from the flexibility of the conductive network, rather than rupturing effect, at 1.5 wt% KB that can sustain higher load of NTO without significant decrease in the conductivity. Fig. S8 displays the morphology and NTO distribution for a selected anolyte (10 wt% NTO–1.5 wt% KB). The optical micrograph demonstrates the homogenous distribution of the NTO particles in the KB conductive network (Fig. S8-a). Deeper insight in the microstructure of the anolyte is gained from the SEM micrograph (Fig. S8-b) which reveals the incorporation of the NTO nanorods in the KB network.

On the other hand,  $G_0$  of the coalesced 2.1 wt% KB dispersion slightly drops upon adding 5 wt% NTO and remains nearly constant until 15 wt% NTO (Fig. 9b). Above this critical concentration,  $G_0$  strongly increases, implying the critical packing conditions [115] beyond which density mismatching or less ordered colloidal crystals [116] emerges. The rod-like morphology of NTO particles may have a significant influence when mixed with nearly spherical coalesced KB aggregates. The initial drop in  $G_0$  is in tandem with a similar decrease in  $\Sigma$  at 5 wt% NTO, beyond which the conductivity of the anolytes does not significantly change at higher NTO content. In comparison to the semi-dilute dispersion, this coalesced dispersion is likely to sustain lesser content of NTO beyond which the network rigidity is strongly increased. It is worth to mention that the anolyte at 30 wt% NTO is enough stiff to be examined by rheology. Therefore, the high rigidity of NTO–2.1 wt% KB suspensions at relatively lower NTO render them inappropriate suspension electrodes for semisolid flow batteries. Indeed, the rheo-electrical properties of suspension electrodes under no flow (static) conditions are not the solely key factor that determines the optimal formulations; however, we expect serious structural transition consistent with loss of suspensions' conductivity under continuous flow conditions. Accordingly, suspension electrodes formulated at 1.5 wt% KB are recommended to investigate their rheo-electrical properties and electrochemical performance under shear flow in order to accurately determine the optimal flow conditions. This is the aim of work in progress in our laboratory.

#### 4. Conclusion

In the current study, we attempt to formulate and rheo-electrically characterize aqueous suspensions composed of carbon black (KB) and sodium titanate ( $\text{Na}_2\text{Ti}_3\text{O}_7$ ; NTO) dispersed in branched micelle solution, as novel aqueous anolytes for semisolid flow batteries. The branched micelle solution interestingly showed wide electrochemical stability window of 3.5 V with relatively low viscosity, rendering it as an excellent aqueous dispersing medium for the formulation of suspension electrodes for aqueous sodium-ion semisolid flow battery. In such unique dispersing medium, the conductive KB particles showed unusual aggregation mechanism controlled by the electrostatic repulsion forces that doubly originate from the inter-aggregate soft interaction and bulk micelle interactions. This remarkable interaction renders the dispersions rheologically percolated at KB content (0.3 wt%) three-times lower than its electrical percolating threshold (0.9 wt%). The peculiar percolation mechanism was mainly described by electrostatically interacting anisometric aggregates, rather than conventional physically connected aggregates. The simultaneous rheo-electrical behavior of KB dispersions revealed shear-induced reorientation (or alignments), rather than physical breaking up of KB network, so that the dispersions unusually resist the loss of electrical conductivity under continuous flow conditions. Above a critical KB content (1.5 wt%), large densified spherical aggregates were structured in coalesced (saturated) network unable to retain their electrical conductivities at high shear rate.

To validate such unique networking picture, NTO-based suspensions were rheo-electrically examined under quiescent condition. The semi-dilute 1.5 wt% KB dispersion could sustain higher load of active material (up to 30 wt% NTO) without severe influence on the rigidity (rheological plateau modulus  $G_0$ ) and electrical conductivity ( $\Sigma$ ) of the suspensions. In contrary, the coalesced KB dispersion could poorly tolerate

lesser NTO content (15 wt% NTO) before it turned stiffer suspension. Based on these findings, further investigation for the rheo-electrical properties and electrochemical performance of optimal NTO–KB suspension electrodes under flow conditions are of worthy significance for novel aqueous sodium-based semisolid redox flow battery applications.

#### CRedit authorship contribution statement

**Mentallah Meslam:** Investigation, Methodology, Data curation, Writing – original draft. **Ahmed A. Elzatahry:** Supervision, Validation, Reviewing. **Mohamed Youssry:** Supervision, Investigation, Resources, Formal analysis, Writing – original draft and reviewing, Funding acquisition.

#### Declaration of Competing Interest

There is no conflict of interest.

#### Acknowledgement

The authors wish to thank staff at the Central Laboratories Unit, Qatar University for accomplishing SEM and Raman spectroscopy, and the staff at the Center for Advanced Materials, Qatar University for performing the XRD measurements. Mohamed Youssry would like to acknowledge the financial support from Qatar University [Grant No. QUST-1-CAS-2020-6]. Open Access funding provided by the Qatar National Library is acknowledged.

#### Appendix A. Supplementary materials

Supplementary data associated with this article can be found in the online version at doi:10.1016/j.colsurfa.2022.129376.

#### References

- [1] Y. Zhao, Y. Ding, Y. Li, L. Peng, H.R. Byon, J.B. Goodenough, G. Yu, A chemistry and material perspective on lithium redox flow batteries towards high-density electrical energy storage, *Chem. Soc. Rev.* 44 (22) (2015) 7968–7996.
- [2] C. Ponce de León, A. Frías-Ferrer, J. González-García, D.A. Szánto, F.C. Walsh, Redox flow cells for energy conversion, *J. Power Sources* 160 (1) (2006) 716–732.
- [3] M. Duduta, B. Ho, V.C. Wood, P. Limthongkul, V.E. Brunini, W.C. Carter, Y. M. Chiang, Semi-solid lithium rechargeable flow battery, *Adv. Energy Mater.* 1 (4) (2011) 511–516.
- [4] S. Hamelet, T. Tzedakis, J.B. Leriche, S. Sailler, D. Larcher, P.L. Taberna, P. Simon, J.M. Tarascon, Non-aqueous Li-based redox flow batteries, *J. Electrochem. Soc.* 159 (8) (2012) A1360–A1367.
- [5] S. Hamelet, D. Larcher, L. Dupont, J.-M. Tarascon, Silicon-based non aqueous anolyte for Li redox-flow batteries, *J. Electrochem. Soc.* 160 (3) (2013) A516.
- [6] M. Youssry, L. Madec, P. Soudan, M. Cerbelaud, D. Guyomard, B. Lestriez, Non-aqueous carbon black suspensions for lithium-based redox flow batteries: rheology and simultaneous rheo-electrical behavior, *Phys. Chem. Chem. Phys.* 15 (34) (2013) 14476–14486.
- [7] M. Youssry, L. Madec, P. Soudan, M. Cerbelaud, D. Guyomard, B. Lestriez, Formulation of flowable anolyte for redox flow batteries: rheo-electrical study, *J. Power Sources* 274 (2015) 424–431.
- [8] L. Madec, M. Youssry, M. Cerbelaud, P. Soudan, D. Guyomard, B. Lestriez, Electronic vs ionic limitations to electrochemical performance in  $\text{Li}_4\text{Ti}_5\text{O}_{12}$ -based organic suspensions for lithium-redox flow batteries, *J. Electrochem. Soc.* 161 (5) (2014) A693–A699.
- [9] I. Ruggeri, C. Arbizzani, F. Soavi, Carbonaceous catholyte for high energy density semi-solid  $\text{Li}/\text{O}_2$  flow battery, *Carbon* 130 (2018) 749–757.
- [10] V. Khomenko, E. Raymundo-Piñero, F. Béguin, Optimisation of an asymmetric manganese oxide/activated carbon capacitor working at 2V in aqueous medium, *J. Power Sources* 153 (1) (2006) 183–190.
- [11] Z. Li, K.C. Smith, Y. Dong, N. Baram, F.Y. Fan, J. Xie, P. Limthongkul, W.C. Carter, Y.-M. Chiang, Aqueous semi-solid flow cell: demonstration and analysis, *Phys. Chem. Chem. Phys.* 15 (38) (2013) 15833–15839.
- [12] E. Ventosa, O. Amedu, W. Schuhmann, Aqueous mixed-cation semi-solid hybrid-flow batteries, *ACS Appl. Energy Mater.* 1 (10) (2018) 5158–5162.
- [13] C. Dong, F. Xu, L. Chen, Z. Chen, Y. Cao, Design strategies for high-voltage aqueous batteries, *Small Struct.* 2 (7) (2021), 2100001.
- [14] Z. Hou, X. Zhang, X. Li, Y. Zhu, J. Liang, Y. Qian, Surfactant widens the electrochemical window of an aqueous electrolyte for better rechargeable aqueous sodium/zinc battery, *J. Mater. Chem. A* 5 (2) (2017) 730–738.

- [15] K.B. Hatzell, M. Boota, Y. Gogotsi, Materials for suspension (semi-solid) electrodes for energy and water technologies, *Chem. Soc. Rev.* 44 (23) (2015) 8664–8687.
- [16] S.P. Ong, V.L. Chevrier, G. Hautier, A. Jain, C. Moore, S. Kim, X. Ma, G. Ceder, Voltage, stability and diffusion barrier differences between sodium-ion and lithium-ion intercalation materials, *Energy Environ. Sci.* 4 (9) (2011) 3680–3688.
- [17] Y. Li, Y. Lu, C. Zhao, Y.-S. Hu, M.-M. Titirici, H. Li, X. Huang, L. Chen, Recent advances of electrode materials for low-cost sodium-ion batteries towards practical application for grid energy storage, *Energy Storage Mater.* 7 (2017) 130–151.
- [18] J.-Y. Hwang, S.-T. Myung, Y.-K. Sun, Sodium-ion batteries: present and future, *Chem. Soc. Rev.* 46 (12) (2017) 3529–3614.
- [19] P. Senguttuvan, G. Rousse, V. Seznec, J.-M. Tarascon, M.R. Palacín,  $\text{Na}_2\text{Ti}_3\text{O}_7$ : Lowest voltage ever reported oxide insertion electrode for sodium ion batteries, *Chem. Mater.* 23 (18) (2011) 4109–4111.
- [20] C. Wu, W. Hua, Z. Zhang, B. Zhong, Z. Yang, G. Feng, W. Xiang, Z. Wu, X. Guo, Design and synthesis of layered  $\text{Na}_2\text{Ti}_3\text{O}_7$  and tunnel  $\text{Na}_2\text{Ti}_6\text{O}_{13}$  hybrid structures with enhanced electrochemical behavior for sodium-ion batteries, *Adv. Sci.* 5 (9) (2018), 1800519.
- [21] Y. Zhang, H. Hou, X. Yang, J. Chen, M. Jing, Z. Wu, X. Jia, X. Ji, Sodium titanate cuboid as advanced anode material for sodium ion batteries, *J. Power Sources* 305 (2016) 200–208.
- [22] X. Sun, Y. Li, Synthesis and characterization of ion-exchangeable titanate nanotubes, *Chem. Eur. J.* 9 (10) (2003) 2229–2238.
- [23] S.W. Holder, S.C. Grant, H. Mohammadigoushki, Nuclear magnetic resonance diffusometry of linear and branched wormlike micelles, *Langmuir* 37 (12) (2021) 3585–3596.
- [24] H. Rehage, H. Hoffmann, Rheological properties of viscoelastic surfactant systems, *J. Phys. Chem.* 92 (16) (1988) 4712–4719.
- [25] S. Wu, H. Mohammadigoushki, Linear versus branched: flow of a wormlike micellar fluid past a falling sphere, *Soft Matter* 17 (16) (2021) 4395–4406.
- [26] L. Madec, M. Yousry, M. Cerbelaud, P. Soudan, D. Guyomard, B. Lestriez, Surfactant for enhanced rheological, electrical, and electrochemical performance of suspensions for semisolid redox flow batteries and supercapacitors, *ChemPlusChem* 80 (2) (2015) 396–401.
- [27] H. Tomiyasu, H. Shikata, K. Takao, N. Asanuma, S. Taruta, Y.-Y. Park, An aqueous electrolyte of the widest potential window and its superior capability for capacitors, *Sci. Rep.* 7 (1) (2017) 1–12.
- [28] D. Evans, J.P. Hart, G. Rees, Voltammetric behaviour of salicylic acid at a glassy carbon electrode and its determination in serum using liquid chromatography with amperometric detection, *Analyst* 116 (8) (1991) 803–806.
- [29] A.A.J. Torriero, J.M. Luco, L. Sereno, J. Raba, Voltammetric determination of salicylic acid in pharmaceuticals formulations of acetylsalicylic acid, *Talanta* 62 (2) (2004) 247–254.
- [30] J. Park, C. Eun, Electrochemical behavior and determination of salicylic acid at carbon-fiber electrodes, *Electrochim. Acta* 194 (2016) 346–356.
- [31] B. Louhichi, N. Bensalash, A. Gadi, Electrochemical oxidation of benzoic acid derivatives on boron doped diamond: Voltammetric study and galvanostatic electrolyses, *Chem. Eng. Technol.* 29 (8) (2006) 944–950.
- [32] W.-D. Zhang, B. Xu, Y.-X. Hong, Y.-X. Yu, J.-S. Ye, J.-Q. Zhang, Electrochemical oxidation of salicylic acid at well-aligned multiwalled carbon nanotube electrode and its detection, *J. Solid State Electrochem.* 14 (9) (2010) 1713–1718.
- [33] K. Xu, Nonaqueous liquid electrolytes for lithium-based rechargeable batteries, *Chem. Rev.* 104 (10) (2004) 4303–4418.
- [34] L. Coustan, D. Bélanger, Electrochemical activity of platinum, gold and glassy carbon electrodes in water-in-salt electrolyte, *J. Electroanal. Chem.* 854 (2019), 113538.
- [35] L. Coustan, G. Shul, D. Bélanger, Electrochemical behavior of platinum, gold and glassy carbon electrodes in water-in-salt electrolyte, *Electrochem. Commun.* 77 (2017) 89–92.
- [36] H. Ao, C. Chen, Z. Hou, W. Cai, M. Liu, Y. Jin, X. Zhang, Y. Zhu, Y. Qian, Electrolyte solvation structure manipulation enables safe and stable aqueous sodium ion batteries, *J. Mater. Chem. A* 8 (28) (2020) 14190–14197.
- [37] Y. Zhang, A. Narayanan, F. Mugele, M.A. Cohen Stuart, M.H.G. Duits, Charge inversion and colloidal stability of carbon black in battery electrolyte solutions, *Colloids Surf., A* 489 (2016) 461–468.
- [38] V. Bal, Coagulation behavior of spherical particles embedded in laminar shear flow in presence of DLVO and non-DLVO forces, *J. Colloid Interface Sci.* 564 (2020) 170–181.
- [39] M.N. Patel, P.G. Smith, J. Kim, T.E. Milner, K.P. Johnston, Electrophoretic mobility of concentrated carbon black dispersions in a low-permittivity solvent by optical coherence tomography, *J. Colloid Interface Sci.* 345 (2) (2010) 194–199.
- [40] Y.-J. Yang, A.V. Kelkar, X. Zhu, G. Bai, H.T. Ng, D.S. Corti, E.I. Franses, Effect of sodium dodecylsulfate monomers and micelles on the stability of aqueous dispersions of titanium dioxide pigment nanoparticles against agglomeration and sedimentation, *J. Colloid Interface Sci.* 450 (2015) 434–445.
- [41] P.K. Singh, J.J. Adler, Y.I. Rabinovich, B.M. Moudgil, Investigation of self-assembled surfactant structures at the solid–liquid interface using FT-IR/ATR, *Langmuir* 17 (2) (2001) 468–473.
- [42] A.A. Zaman, P. Singh, B.M. Moudgil, Impact of self-assembled surfactant structures on rheology of concentrated nanoparticle dispersions, *J. Colloid Interface Sci.* 251 (2) (2002) 381–387.
- [43] T. Tadros, Interparticle interactions in concentrated suspensions and their bulk (Rheological) properties, *Adv. Colloid Interface Sci.* 168 (1) (2011) 263–277.
- [44] K. Hyun, S.H. Kim, K.H. Ahn, S.J. Lee, Large amplitude oscillatory shear as a way to classify the complex fluids, *J. Non-Newton. Fluid Mech.* 107 (1) (2002) 51–65.
- [45] M. Yousry, D. Guyomard, B. Lestriez, Suspensions of carbon nanofibers in organic medium: rheo-electrical properties, *Phys. Chem. Chem. Phys.* 17 (48) (2015) 32316–32327.
- [46] M. Yousry, F.Z. Kamand, M.I. Magzoub, M.S. Nasser, Aqueous dispersions of carbon black and its hybrid with carbon nanofibers, *RSC Adv.* 8 (56) (2018) 32119–32131.
- [47] H. Asai, A. Masuda, M. Kawaguchi, Rheological properties of colloidal gels formed from fumed silica suspensions in the presence of cationic surfactants, *J. Colloid Interface Sci.* 328 (1) (2008) 180–185.
- [48] V. Calabrese, S. Varchanis, S.J. Haward, J. Tsamopoulos, A.Q. Shen, Structure-property relationship of a soft colloidal glass in simple and mixed flows, *J. Colloid Interface Sci.* 601 (2021) 454–466.
- [49] G.J. Donley, P.K. Singh, A. Shetty, S.A. Rogers, Elucidating the  $G''$  overshoot in soft materials with a yield transition via a time-resolved experimental strain decomposition, *PNAS* 117 (36) (2020) 21945–21952.
- [50] A. Mujumdar, A.N. Beris, A.B. Metzner, Transient phenomena in thixotropic systems, *J. Non-Newton. Fluid Mech.* 102 (2) (2002) 157–178.
- [51] W.-H. Shih, W.Y. Shih, S.-I. Kim, J. Liu, I.A. Aksay, Scaling behavior of the elastic properties of colloidal gels, *Phys. Rev. A* 42 (8) (1990) 4772–4779.
- [52] F. Khalkhal, A.S. Negi, J. Harrison, C.D. Stokes, D.L. Morgan, C.O. Osuji, Evaluating the dispersant stabilization of colloidal suspensions from the scaling behavior of gel rheology and adsorption measurements, *Langmuir* 34 (3) (2018) 1092–1099.
- [53] S.S. Rahatekar, K.K. Koziol, S.R. Kline, E.K. Hobbie, J.W. Gilman, A.H. Windle, Length-dependent mechanics of carbon-nanotube networks, *Adv. Mater.* 21 (8) (2009) 874–878.
- [54] L.A. Hough, M.F. Islam, P.A. Janmey, A.G. Yodh, Viscoelasticity of single wall carbon nanotube suspensions, *Phys. Rev. Lett.* 93 (16) (2004), 168102.
- [55] V. Trappe, D. Weitz, Scaling of the viscoelasticity of weakly attractive particles, *Phys. Rev. Lett.* 85 (2) (2000) 449.
- [56] M.L. Gardel, J.H. Shin, F.C. MacKintosh, L. Mahadevan, P.A. Matsudaira, D. A. Weitz, Scaling of F-actin network rheology to probe single filament elasticity and dynamics, *Phys. Rev. Lett.* 93 (18) (2004), 188102.
- [57] J. Appel, B. Fölker, J. Sprakel, Mechanics at the glass-to-gel transition of thermoresponsive microgel suspensions, *Soft Matter* 12 (9) (2016) 2515–2522.
- [58] R. Niu, J. Gong, D. Xu, T. Tang, Z.-Y. Sun, Rheological properties of ginger-like amorphous carbon filled silicon oil suspensions, *Colloids Surf. A* 444 (2014) 120–128.
- [59] M. Kawaguchi, M. Okuno, T. Kato, Rheological properties of carbon black suspensions in a silicone oil, *Langmuir* 17 (20) (2001) 6041–6044.
- [60] A.J.W. ten Brinke, L. Bailey, H.N.W. Lekkerkerker, G.C. Maitland, Rheology modification in mixed shape colloidal dispersions. Part I: pure components, *Soft Matter* 3 (9) (2007) 1145–1162.
- [61] D.B. Genovese, Shear rheology of hard-sphere, dispersed, and aggregated suspensions, and filler-matrix composites, *Adv. Colloid Interface Sci.* 171 (2012) 1–16.
- [62] S. Lazzari, L. Nicoud, B. Jaquet, M. Lattuada, M. Morbidelli, Fractal-like structures in colloid science, *Adv. Colloid Interface Sci.* 235 (2016) 1–13.
- [63] J.J. Richards, J.B. Hipp, J.K. Riley, N.J. Wagner, P.D. Butler, Clustering and percolation in suspensions of carbon black, *Langmuir* 33 (43) (2017) 12260–12266.
- [64] F. Coupette, L. Zhang, B. Kuttich, A. Chumakov, S.V. Roth, L. González-García, T. Kraus, T. Schilling, Percolation of rigid fractal carbon black aggregates, *J. Chem. Phys.* 155 (12) (2021), 124902.
- [65] J.J. Adler, P.K. Singh, A. Patist, Y.I. Rabinovich, D.O. Shah, B.M. Moudgil, Correlation of particulate dispersion stability with the strength of self-assembled surfactant films, *Langmuir* 16 (18) (2000) 7255–7262.
- [66] P.-J. Lu, J.C. Conrad, H.M. Wyss, A.B. Schofield, D.A. Weitz, Fluids of clusters in attractive colloids, *Phys. Rev. Lett.* 96 (2) (2006), 028306.
- [67] F. Khalkhal, P.J. Carreau, Scaling behavior of the elastic properties of non-dilute MWCNT-epoxy suspensions, *Rheol. Acta* 50 (9) (2011) 717–728.
- [68] R. Buscall, P.D.A. Mills, J.W. Goodwin, D.W. Lawson, Scaling behaviour of the rheology of aggregate networks formed from colloidal particles, *J. Chem. Soc. Faraday Trans. 1* 84 (12) (1988) 4249–4260.
- [69] M. Chen, W.B. Russel, Characteristics of flocculated silica dispersions, *J. Colloid Interface Sci.* 141 (2) (1991) 564–577.
- [70] E. Dickinson, Structure and rheology of simulated gels formed from aggregated colloidal particles, *J. Colloid Interface Sci.* 225 (1) (2000) 2–15.
- [71] E. Dickinson, Structure and rheology of colloidal particle gels: Insight from computer simulation, *Adv. Colloid Interface Sci.* 199–200 (2013) 114–127.
- [72] M.L. Eggersdorfer, D. Kadau, H.J. Herrmann, S.E. Pratsinis, Multiparticle sintering dynamics: from fractal-like aggregates to compact structures, *Langmuir* 27 (10) (2011) 6358–6367.
- [73] R. Jullien, P. Meakin, Simple models for the restructuring of three-dimensional ballistic aggregates, *J. Colloid Interface Sci.* 127 (1) (1989) 265–272.
- [74] S. Jungblut, J.-O. Joswig, A. Eychmüller, Diffusion- and reaction-limited cluster aggregation revisited, *Phys. Chem. Chem. Phys.* 21 (10) (2019) 5723–5729.
- [75] Y. Aoki, A. Hatano, H. Watanabe, Rheology of carbon black suspensions. II. Well dispersed system, *Rheol. Acta* 42 (4) (2003) 321–325.
- [76] A. Narayanan, F. Mugele, M.H. Duits, Mechanical history dependence in carbon black suspensions for flow batteries: a rheo-impedance study, *Langmuir* 33 (7) (2017) 1629–1638.
- [77] C. Penu, G.H. Hu, A. Fernandez, P. Marchal, L. Choplin, Rheological and electrical percolation thresholds of carbon nanotube/polymer nanocomposites, *Polym. Eng. Sci.* 52 (10) (2012) 2173–2181.

- [78] F. Du, R.C. Scogna, W. Zhou, S. Brand, J.E. Fischer, K.I. Winey, Nanotube networks in polymer nanocomposites: Rheology and electrical conductivity, *Macromolecules* 37 (24) (2004) 9048–9055.
- [79] M.D. Lima, M.J. Andrade, V. Skákalová, C.P. Bergmann, S. Roth, Dynamic percolation of carbon nanotubes in liquid medium, *J. Mater. Chem.* 17 (46) (2007) 4846–4853.
- [80] M. Sahimi, B.D. Hughes, L.E. Scriven, H.T. Davis, Critical exponent of percolation conductivity by finite-size scaling, *J. Phys. C* 16 (16) (1983) L521–L527.
- [81] C.A. Martin, J.K.W. Sandler, M.S.P. Shaffer, M.K. Schwarz, W. Bauhofer, K. Schulte, A.H. Windle, Formation of percolating networks in multi-wall carbon-nanotube-epoxy composites, *Compos. Sci. Technol.* 64 (15) (2004) 2309–2316.
- [82] A. Yu, M.E. Itkis, E. Bekyarova, R.C. Haddon, Effect of single-walled carbon nanotube purity on the thermal conductivity of carbon nanotube-based composites, *Appl. Phys. Lett.* 89 (13) (2006), 133102.
- [83] D. Stauffer, A. Aharony, *Introduction to Percolation Theory*, Taylor & Francis, London, 1992.
- [84] B.G. Soares, K.M.N. Gamboa, A.J.B. Ferreira, E. Ueti, S.S. Camargo Jr., Effect of the mold temperature on the electrical properties of carbon-black-loaded polystyrene/SB block copolymer blends, *J. Appl. Polym. Sci.* 69 (4) (1998) 825–833.
- [85] W. Bauhofer, J.Z. Kovacs, A review and analysis of electrical percolation in carbon nanotube polymer composites, *Compos. Sci. Technol.* 69 (10) (2009) 1486–1498.
- [86] I. Balberg, Tunneling and nonuniversal conductivity in composite materials, *Phys. Rev. Lett.* 59 (12) (1987) 1305–1308.
- [87] S. Vionnet-Menot, C. Grimaldi, T. Maeder, S. Strässler, P. Ryser, Tunneling-percolation origin of nonuniversality: Theory and experiments, *Phys. Rev. B* 71 (6) (2005), 064201.
- [88] D. Toker, D. Azulay, N. Shimoni, I. Balberg, O. Millo, Tunneling and percolation in metal-insulator composite materials, *Phys. Rev. B* 68 (4) (2003), 041403.
- [89] A. Brilloni, F. Poli, G.E. Spina, D. Genovese, G. Pagnotta, F. Soavi, Improving the electrical percolating network of carbonaceous slurries by superconcentrated electrolytes: An electrochemical impedance spectroscopy study, *ACS Appl. Mater. Interfaces* 13 (11) (2021) 13872–13882.
- [90] G.N. Choi, I.M. Krieger, Rheological studies on sterically stabilized model dispersions of uniform colloidal spheres: II. Steady-shear viscosity, *J. Colloid Interface Sci.* 113 (1) (1986) 101–113.
- [91] J. Mewis, J. Vermant, Rheology of sterically stabilized dispersions and latices, *Prog. Org. Coat.* 40 (1) (2000) 111–117.
- [92] C.L. Barrie, P.C. Griffiths, R.J. Abbott, I. Grillo, E. Kudryashov, C. Smyth, Rheology of aqueous carbon black dispersions, *J. Colloid Interface Sci.* 272 (1) (2004) 210–217.
- [93] V. Grenard, N. Taberlet, S. Manneville, Shear-induced structuration of confined carbon black gels: steady-state features of vorticity-aligned flocs, *Soft Matter* 7 (8) (2011) 3920–3928.
- [94] C.O. Osuji, C. Kim, D.A. Weitz, Shear thickening and scaling of the elastic modulus in a fractal colloidal system with attractive interactions, *Phys. Rev. E* 77 (6) (2008), 060402.
- [95] R. Mari, R. Seto, J.F. Morris, M.M. Denn, Shear thickening, frictionless and frictional rheologies in non-Brownian suspensions, *J. Rheol.* 58 (6) (2014) 1693–1724.
- [96] R.V. More, A.M. Ardekani, Unifying disparate rate-dependent rheological regimes in non-Brownian suspensions, *Phys. Rev. E* 103 (6) (2021), 062610.
- [97] P. D'Haene, J. Mewis, Rheological characterization of bimodal colloidal dispersions, *Rheol. Acta* 33 (3) (1994) 165–174.
- [98] J.F. Morris, Lubricated-to-frictional shear thickening scenario in dense suspensions, *Phys. Rev. Fluids* 3 (11) (2018), 110508.
- [99] J.R. Melrose, R.C. Ball, Continuous shear thickening transitions in model concentrated colloids—the role of interparticle forces, *J. Rheol.* 48 (5) (2004) 937–960.
- [100] J.R. Melrose, J.H. van Vliet, R.C. Ball, Continuous shear thickening and colloid surfaces, *Phys. Rev. Lett.* 77 (22) (1996) 4660–4663.
- [101] T.F. Tadros, *Rheology of Dispersions: Principles and Applications*, John Wiley & Sons, 2011.
- [102] E. Brown, N.A. Forman, C.S. Orellana, H. Zhang, B.W. Maynor, D.E. Betts, J. M. DeSimone, H.M. Jaeger, Generality of shear thickening in dense suspensions, *Nat. Mater.* 9 (3) (2010) 220–224.
- [103] E. Brown, H.M. Jaeger, Shear thickening in concentrated suspensions: phenomenology, mechanisms and relations to jamming, *Rep. Prog. Phys.* 77 (4) (2014), 046602.
- [104] X. Cheng, J.H. McCoy, J.N. Israelachvili, I. Cohen, Imaging the microscopic structure of shear thinning and thickening colloidal suspensions, *Science* 333 (6047) (2011) 1276–1279.
- [105] H.M. Laun, Normal stresses in extremely shear thickening polymer dispersions, *J. Non-Newton. Fluid Mech.* 54 (1994) 87–108.
- [106] A.A. Catherall, J.R. Melrose, R.C. Ball, Shear thickening and order–disorder effects in concentrated colloids at high shear rates, *J. Rheol.* 44 (1) (2000) 1–25.
- [107] B.J. Maranzano, N.J. Wagner, Flow-small angle neutron scattering measurements of colloidal dispersion microstructure evolution through the shear thickening transition, *J. Chem. Phys.* 117 (22) (2002) 10291–10302.
- [108] V.T. O'Brien, M.E. Mackay, Stress components and shear thickening of concentrated hard sphere suspensions, *Langmuir* 16 (21) (2000) 7931–7938.
- [109] B. Kaffashi, V.T. O'Brien, M.E. Mackay, S.M. Underwood, Elastic-like and viscous-like components of the shear viscosity for nearly hard sphere, brownian suspensions, *J. Colloid Interface Sci.* 187 (1) (1997) 22–28.
- [110] S.R. Waitukaitis, H.M. Jaeger, Impact-activated solidification of dense suspensions via dynamic jamming fronts, *Nature* 487 (7406) (2012) 205–209.
- [111] X. Xu, S.A. Rice, A.R. Dinner, Relation between ordering and shear thinning in colloidal suspensions, *PNAS* 110 (10) (2013) 3771–3776.
- [112] G.Y. Onoda, E.G. Liniger, Random loose packings of uniform spheres and the dilatancy onset, *Phys. Rev. Lett.* 64 (22) (1990) 2727–2730.
- [113] B.L. Ellis, L.F. Nazar, Sodium and sodium-ion energy storage batteries, *Curr. Opin. Solid State Mater. Sci.* 16 (4) (2012) 168–177.
- [114] P. Mongondry, C.W. Macosko, T. Moaddel, Rheology of highly concentrated anionic surfactants, *Rheol. Acta* 45 (6) (2006) 891–898.
- [115] S.M. Olhero, J.M.F. Ferreira, Influence of particle size distribution on rheology and particle packing of silica-based suspensions, *Powder Technol.* 139 (1) (2004) 69–75.
- [116] Z. Zhou, P.J. Scales, D.V. Boger, Chemical and physical control of the rheology of concentrated metal oxide suspensions, *Chem. Eng. Sci.* 56 (9) (2001) 2901–2920.